



# A multi-scale high-resolution analysis of global sea surface temperature<sup>☆</sup>



Toshio Michael Chin<sup>\*</sup>, Jorge Vazquez-Cuervo, Edward M. Armstrong

*Jet Propulsion Laboratory, California Institute of Technology, 4800 Oak Grove Drive, Pasadena, CA 91109, USA*

## ARTICLE INFO

### Keywords:

Sea surface temperature  
Multi-sensor  
Multi-scale  
Wavelet

## ABSTRACT

The Multi-scale Ultra-high Resolution (MUR) sea surface temperature (SST) analysis presents daily SST estimates on a global  $0.01^\circ \times 0.01^\circ$  grid. The current version (Version 4.1, <http://dx.doi.org/10.5067/GHGMR-4FJ04>) features the 1-km resolution MODIS retrievals, which are fused with AVHRR GAC, microwave, and in-situ SST data by applying internal correction for relative biases among the data sets. Only the night-time (dusk to dawn locally) satellite SST retrievals are used to estimate the foundation SST. The MUR SST values agree with the GHRSST Multi-Product Ensemble (GMPE) SST field to  $0.36^\circ\text{C}$  on average, except in summer-time Arctic region where the existing SST analysis products are known to disagree with each other. The feature resolution of the MUR SST analysis is an order of magnitude higher than most existing analysis products.

The Multi-Resolution Variational Analysis (MRVA) method allows the MUR analysis to use multiple synoptic time scales, including a 5-day data window used for reconstruction of mesoscale features and data windows of only few hours for the smaller scale features. Reconstruction of fast evolving small scale features and interpolation over persistent large data voids can be achieved simultaneously by the use of multiple synoptic windows in the multi-scale setting. The MRVA method is also a “mesh-less” interpolation procedure that avoids truncation of the geolocation data during gridding and binning of satellite samples. Future improvements of the MUR SST analysis will include ingestion of day-time MODIS retrievals as well as more recent high-resolution SST retrievals from VIIRS.

## 1. Introduction

Retrievals from satellite infra-red sensors can sample global sea surface temperature (SST) at a spatial resolution of 1 km or finer. Examples are the Moderate Resolution Imaging Spectroradiometer (MODIS) aboard Terra and Aqua satellites, the Advanced Along Track Scanning Radiometer (AATSR) aboard Envisat, the Visible Infrared Imaging Radiometer Suite (VIIRS) on Suomi NPP satellite, and the Advanced Very High Resolution Radiometer (AVHRR) on various space platforms.

Until recently, high-resolution information from these sensors is rarely used in gridded multi-sensor SST analysis. In existing daily global SST analysis products, typical grid resolution ranges from  $0.05^\circ \times 0.05^\circ$  to  $0.25^\circ \times 0.25^\circ$ , or approximately from 5 to 25 km (e.g., Reynolds and Smith, 1994; Brasnett, 2008; Donlon et al., 2012). Due to spatial and temporal averaging applied for interpolation, actual resolution of the physical features can be substantially coarser than the grid resolutions (Reynolds and Chelton, 2010; Reynolds et al., 2013), often just enough to resolve ocean mesoscale features. Some of the SST analysis fields may

be intentionally smoothed to satisfy operational requirements, such as dynamical compatibility with a numerical weather prediction model that uses the SST analysis as a boundary condition.

The space-time sampling rate sets a fundamental limit on the physical resolution of the analyzed SST field. In particular, small scale features can evolve substantially in the course of a day, but the sensor sampling at present is not dense enough for a sub-daily global analysis at a high spatial resolution. Nevertheless, oceanographically useful sub-mesoscale features are available in retrieval data sets, especially those from wide-swath sensors such as MODIS and VIIRS. To capture these small scale features in a gridded analysis, Reynolds et al. (2013) suggest that “the best way forward may be the development of an improved analysis [that] would have high resolution of small-scale features in regions of good coverage and lower resolution in regions of poor coverage.”

The Multi-scale Ultra-high Resolution (MUR) SST analysis is a global daily analysis gridded at a  $0.01^\circ \times 0.01^\circ$  horizontal resolution. The MUR analysis ingests the MODIS retrievals (with future plans to include other high-resolution data like the VIIRS retrievals) and seeks to

<sup>☆</sup> Copyright 2016 California Institute of Technology. Government sponsorship acknowledged.

<sup>\*</sup> Corresponding author.

E-mail address: [mike.chin@jpl.nasa.gov](mailto:mike.chin@jpl.nasa.gov) (T.M. Chin).

URL: <http://mur.jpl.nasa.gov> (T.M. Chin).

**Table 1**

The SST data sources for the MUR analysis and the data-specific analysis parameters. The sample size ( $N$ ) is a nominal value after quality screening and selection of night-time samples in the multi-day window. The upper value in the “scale range” column indicates the highest possible analysis resolution  $L$  for the given data type.

Data type	Input data			Analysis parameters	
	Data set	Resolution	Size ( $N$ )	Window	Scale range
High-resolution infra-red	MODIS Terra	1 km	$1 \cdot 10^8$	5 days	$0 \leq \ell < 10$
	MODIS Aqua	1 km	$1 \cdot 10^8$		
AVHRR infra-red	Pathfinder Night	5 km	$5 \cdot 10^6$	5 days	$0 \leq \ell < 7$
	Pathfinder Day	5 km	$5 \cdot 10^6$		
	NOAA-18 GAC	9 km	$5 \cdot 10^6$		
	NOAA-19 GAC	9 km	$5 \cdot 10^6$		
	MetOp-A GAC	9 km	$5 \cdot 10^6$		
Microwave	AMSR-E	25 km	$2 \cdot 10^7$	5 days	$0 \leq \ell < 6$
	WindSat	25 km	$2 \cdot 10^6$		
	AMSR2	25 km	$4 \cdot 10^6$		
	iQuam	point-wise	$2 \cdot 10^5$		
In-situ	OSI-409/401	10 km	Seasonal	7 days	$0 \leq \ell < 4$
Ice fraction				1 day	$0 \leq \ell < 7$

capture small scale SST structures wherever available. The MODIS data are combined with lower resolution SST data from satellite infra-red and microwave sensors as well as in-situ measurements. The *foundation* SST, or bulk near-surface temperature free of diurnal variations due to solar heating (Donlon et al., 2007), is estimated by using only the night-time (dusk to dawn locally) samples from the satellite retrievals. The current version (Version 4.1) of MUR SST analysis has a temporal coverage from 1 June 2002 to the present, approximately coinciding with the microwave SST retrieval era. Its high resolution SST features have found scientific applications in: coastal air-sea interactions and phenomena (Nidzieko and Largier, 2013; Turrent and Zaitsev, 2014; Wiafe and Nyadjro, 2015; Chen et al., 2015; Gentemann et al., 2017), atmosphere-ocean coupled model (Iwasaki et al., 2014), tidal mixing (Ray and Susanto, 2016), identification/tracking of surface structures (Bashmachnikov et al., 2013; Vazquez et al., 2013; Liu et al., 2015; Mill et al., 2015), and determination of physical indicators for bio-productivity (Goela et al., 2014; Baylis et al., 2015; Scales et al., 2015).

The MUR analysis (hereafter “MUR” for brevity) must combine SST data sets whose inherent spatial scales differ by several orders of magnitudes, ranging from the MODIS samples with 1-km resolution to the buoys spaced by several 100 km. Retrievals from orbiting sensors are collected over a certain period of time to form a synoptic analysis. While a period of several days has been shown appropriate to capture and reconstruct the mesoscale SST features (Reynolds and Smith, 1994; Brasnett, 2008; Donlon et al., 2012), a much shorter time window (e.g., shorter than a day) would be desirable to match the evolution speed of smaller scale features observable in the MODIS data. MUR thus employs a multi-scale data fusion and interpolation technique, called the Multi-Resolution Variational Analysis (MRVA) method, that expands the analysis into additive components based on the scale. This technique allows multiple “synoptic” time-windows to be applied to a single retrieval data set. In particular, a multi-day window can be used to form the mesoscale analysis components, while a sub-day window length can be used for the finer-scale analysis components. Contribution by each data set to the overall analysis can be controlled depending on the inherent resolution of the data set. For example, the buoy data set will not participate in the analysis of the sub-mesoscale components because of its relatively low spatial resolution.

This paper describes the MUR analysis and MRVA method. The MRVA method was first developed to fuse wind vector data sets (Chin et al., 1998). The version of MRVA described here introduces the use of scale-dependent time-windows. Another attribute of MRVA is that it is a mesh-less interpolation method which can avoid the use of spatial binning that distorts the geolocation of the retrieval samples and hence the shape of the analyzed SST (Chin et al., 2014). Section 2 of the paper describes the data sets ingested by the MUR SST analysis and the pre-processing procedures applied to them. Section 3 presents the MRVA method and the analysis procedures. Section 4 then examines the

analyzed SST field and its multi-scale aspects by comparison to other SST data sets. Section 5 concludes the paper with a summary and a list of potential topics of further developments.

## 2. Data sets

MUR combines three types of satellite SST retrieval data sets: infra-red SST retrievals at high resolutions of around 1 km, AVHRR (infra-red) SST retrievals at medium resolution of 4 to 8.8 km, and microwave SST retrievals with a nominal sampling interval of 25 km. The 1-km high-resolution data are the main source of the small-scale SST features observable in MUR and are currently provided by the MODIS sensors. The medium-resolution AVHRR Global Area Coverage (GAC) data are ingested for their relative spatial stability (Table 3, Section 4) within the daily synoptic window. The microwave data are less prone to cloud and water vapor contamination than infra-red SST retrievals and are used to reduce the data voids in the infra-red retrievals. In addition to these three types of satellite data, MUR ingests two types of non-satellite SST data sets: in-situ SST measurements to improve estimation of the foundation temperature, and SST values derived from ice concentration data sets in the polar regions. Table 1 lists these five data types and the data sets ingested by MUR. At least one data set represents each of the five data types at any given time in the MUR SST analysis (Fig. 1).

The Group for High Resolution Sea Surface Temperature (GHRSSST; Donlon et al., 2007) has defined a standard for the contents and formats for the satellite SST data sets. For satellite retrieval products, the standard contents under the GHRSSST convention include the

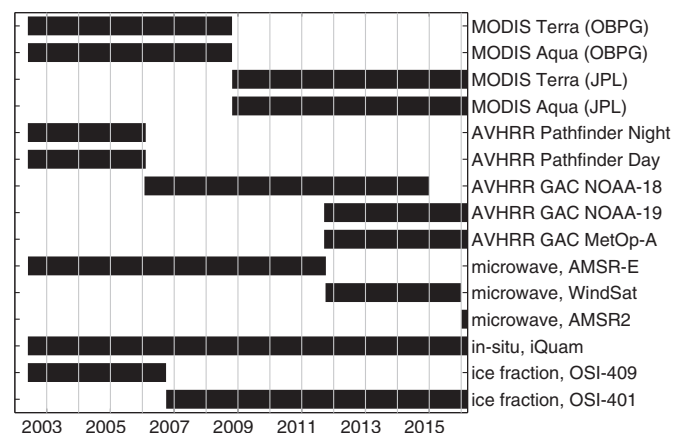


**Fig. 1.** Input data sets used by Version 4.1 of the MUR SST analysis and the period of usage for each data set (horizontal bars). The vertical lines denote the starts of the indicated calendar years.

geolocation, time, uncertainty estimates (bias and precision), and quality flags, along with the SST value for each sample. All satellite SST data used by MUR are GHRSSST data, except for the early MODIS and AVHRR data as detailed below.

### 2.1. High-resolution infra-red retrievals

The MODIS radiometers are on board the Terra and Aqua satellites launched respectively in 1999 and 2002 by NASA to study global dynamics of the Earth's atmosphere, land, and oceans. For SST, the 4, 11, and 12  $\mu\text{m}$  infra-red bands are used with a multi-channel cloud detection scheme (Frey et al., 2008). The observation has a 2300 km-wide swath which allows a nearly full global coverage in one day.

The MODIS SST samples are grouped into the “day time” and “night time” data files depending on whether the measurements are made along the ascending or descending satellite tracks, respectively. MUR uses both types of data and makes its own classification of night-time data based on the sample time and local sunrise/sunset times (Section 2.6.2). Only such night-time samples are ingested by the current version of MUR.

The production of the MODIS SST retrieval data is a collaboration among University of Miami Rosenstiel School of Marine and Atmospheric Science (RSMAS), NASA Ocean Biology Processing Group (OBPG), and NASA Jet Propulsion Laboratory (JPL). At the time of production, the MODIS data in the GHRSSST format were available only for the recent years. For the earlier dates going back to year 2002, OBPG provided non-GHRSSST data (in HDF format) which included quality flags but not the uncertainty estimates (see Section 2.6.3). In the current version of MUR, the MODIS data dated on and before 25 October 2008 are the non-GHRSSST version from OBPG.

Pre-2008 MODIS data complete with GHRSSST-standard uncertainty estimates are now available from OBPG and are to be ingested by a future version of MUR, which also plans to ingest VIIRS data (available since 2013). The VIIRS retrievals could also provide high resolution SST samples in a 3000 km-wide swath and at a sub-km resolution near nadir. The MODIS and VIIRS sensors uniquely captures the 1 km-scale SST features by their wide swaths and global coverages.

## 2.2. AVHRR GAC infra-red retrievals

### 2.2.1. AVHRR GAC sensor data sets

The AVHRR sensors are on the National Oceanic and Atmospheric Administration (NOAA) Polar Orbiting Environmental Satellites (POES) with an operational legacy that traces back to the Television Infrared Observation Satellite-N (TIROS-N) launched in 1978. The MetOp-A/B satellite launched by the European Space Agency (ESA) and the European Organisation for the Exploitation of Meteorological Satellites (EUMETSAT) also carries an AVHRR sensor identical to those on NOAA's POES. The SST values are typically derived using the 11 and 12  $\mu\text{m}$  channels, sometimes in combination with the 3.7  $\mu\text{m}$  channel (e.g., Petrenko et al., 2014). The highest ground resolution that can be obtained from the current AVHRR instruments is 1.1 km at nadir.

The AVHRR data are acquired in three formats: High Resolution Picture Transmission (HRPT), Local Area Coverage (LAC), and Global Area Coverage (GAC). The HRPT data are full resolution data transmitted to a ground station as they are collected. The LAC data are also full resolution data, but the acquisition is recorded with an on-board tape recorder for subsequent transmission during a station overpass. The GAC data are derived from an on-board sample averaging, where four out of every five samples along the scan line are used to compute an average value, and the data from only every third scan line are processed, yielding an effective 4 km resolution at nadir. Further binning and averaging of these pixels result in the final GAC dataset resolution of 8.8 km.

The AVHRR retrievals used by MUR are all GAC data sets. They are produced by the US Naval Oceanographic Office (NAVO) based on the

measurements from NOAA-18, NOAA-19, and MetOp-A satellites. The NOAA-18 data used are dated from 25 January 2006 to 29 December 2014, while both the NOAA-19 and MetOp-A data used are dated from 15 September 2011 to the present (Fig. 1). The high-resolution AVHRR data (LAC and HRPT) are not ingested by MUR at present because of their sub-global (regional) scopes.

### 2.2.2. Pathfinder gridded multi-sensor data sets

At production time, no GHRSSST-format AVHRR GAC data set was available for the early dates of MUR. In place of the AVHRR GAC data from individual sensors for these dates, MUR uses the Pathfinder data set derived from multi-sensor AVHRR GAC retrievals. The Pathfinder data set is used from 1 June 2002 to 9 February 2006. The Pathfinder product ingested by MUR includes quality flags but not the two uncertainty estimates (Section 2.6.3) required by the GHRSSST format. Thus a non-GHRSSST version of the Pathfinder product was used by the current version of MUR.

The AVHRR Pathfinder SST data set is a reanalysis of historical AVHRR data aimed to improve long-term cross-platform consistency by re-calibration of retrieval parameters and is developed jointly by NOAA National Center for Environmental Information (NCEI) and RSMAS (Kilpatrick et al., 2001; Casey et al., 2010). The Pathfinder SST product uses the AVHRR GAC data derived from an on-board sample averaging, yielding an effective 4 km resolution at nadir as described previously. Instead of performing further binning and averaging, the SST data are projected onto a 4-km ( $0.042^\circ \times 0.042^\circ$ ) resolution grid. The GAC data from the NOAA-7, -9, -11, -14, -16, -17, and -18 satellites are used to produce the Pathfinder Version 5.2 data set used by MUR. Pathfinder also provides separate daily gridding for the “daytime” (ascending tracks) and “nighttime” (descending tracks) data, both of which are used by MUR.

The version of Pathfinder data set has some known bias issues (O'Carroll et al., 2012). Future versions of MUR will replace the Pathfinder data with single-sensor AVHRR GAC data as the latter become available (Ignatov et al., 2016). Such single-sensor data sets potentially contain more authentic geolocation information since they are not gridded.

## 2.3. Microwave retrievals

The SST data from infra-red sensors including MODIS and AVHRR have systematic data voids due to cloud contamination which can be geographically and seasonally persistent. Microwave sensors are less prone to such cloud interference and are hence able to provide more stable spatio-temporal coverage. Despite near-shore voids due to land interference (no useful SST sample within 100 km from the coast due to side-lobe contamination) and relatively low 25-km resolution, microwave-based SST data can thus make contributions complementary to those of infra-red SST retrievals.

The microwave SST data sets used by MUR are retrieved from the following three sensors: the Advanced Microwave Scanning Radiometer (AMSR-E) developed by the National Space Development Agency of Japan (NASDA, now JAXA) aboard NASA Aqua satellite launched in May 2002, the WindSat Polarimetric Radiometer developed by the Naval Research Laboratory (NRL) and launched on 6 January 2003 aboard the Department of Defense Coriolis satellite, and the Advanced Microwave Scanning Radiometer 2 (AMSR2) launched on 18 May 2012 aboard the Global Change Observation Mission Water (GCOM-W) satellite developed by the Japan Aerospace Exploration Agency (JAXA).

MUR uses the AMSR-E SST data from the beginning of the analysis to 4 October 2011 when the sensor is lost, the WindSat SST data from 1 October 2011 to 31 December 2015, and the AMSR2 SST data from 1 January 2016 to the present. The Remote Sensing Systems (REMSS) produces these SST data for the GHRSSST project. REMSS releases the microwave SST data products in two stages: a “near-real-time” product which is typically made available within 3 h of measurement reception

and a “final” product typically released within 2 days and containing more accurate retrievals based on atmospheric analysis data including the wind direction from the National Center for Environmental Prediction (NCEP) Final Operational Global Analysis. MUR ingests the “final” version based on availability (see [Section 3.5](#)).

#### 2.4. In situ SST data

The in-situ SST data provide direct measurements of the bulk SST which approximates the foundation SST in current practice. All in-situ SST data ingested by MUR are obtained from the iQuam data set ([Xu and Ignatov, 2010](#)) produced at the Center for Satellite Applications and Research (STAR) in National Environmental Satellite Data and Information Service (NESDIS). The iQuam production system obtains the in-situ SST data from the NCEP Global Telecommunications System (GTS) every 12 h, to perform near-real-time quality-control of SST measurements from ships, drifters, and moorings. The data set is continued to be updated within several days of the measurements. MUR downloads the updated iQuam files daily for the two most recent days. MUR ingests a 7-day composite of iQuam data.

The in-situ SST data originate collectively in highly heterogeneous measurement and transmission conditions. The iQuam system performs quality control based on the following five general procedures ([Xu and Ignatov, 2010](#)): “prescreening” to remove duplicate samples and unrecognizable records; “plausibility check” to see if the stated geolocations are consistent as continuous ship/drifter tracks, etc.; “internal consistency check” to detect outliers in SST time series; “mutual consistency check” to examine consistency among near-coincident SST values from different platforms; “external consistency check” to examine consistency against an independent SST field. An additional check on cross-platform consistency is also performed.

#### 2.5. Ice concentration data

The ice concentration data from satellite microwave sensors are used to locate icy sea surfaces and infer bulk temperature on such high-latitude surfaces where SST retrievals are generally scarce or absent due in part to persistent atmospheric conditions.

MUR uses a daily sea ice concentration data products provided by the EUMETSAT Ocean and Sea Ice Satellite Application Facility (OSI SAF). Ice concentration products are derived from passive microwave satellite measurements by regression of brightness temperature values from multiple frequency and polarization channels ([Andersen et al., 2006](#)). For the OSI SAF sea ice algorithms ([Breivik et al., 2001](#)), the regression coefficients are obtained empirically from a defined set of brightness temperature observations, referred to as *algorithm tie points*, over areas of known sea ice conditions. A Bayesian approach is then used to optimally combine sensor specific data products onto a 10 km polar stereographic projection grid for each 24 h period. The resulting sea ice fields are available daily by around 0600 UTC each day. The sea ice products are delivered separately for the Northern and Southern Hemispheres with confidence flags.

MUR uses two different ice concentration products, Operational Global Sea Ice Concentration (OSI-401) and Global Sea Ice Concentration Reprocessing Data (OSI-409), in order to cover the duration from mid-2002 to the present. The OSI-401 product is operational since March 2005. The OSI-409 product is available from 1987 through 2009 (recently extended to April 2015). MUR uses OSI-401 from the present back to 1 October 2006 and uses OSI-409 prior to that date. The OSI-401 and OSI-409 products differ in the way that the open-water and closed-ice tie-points are determined. OSI-409 uses a dynamical 30-day moving window tie-points, while OSI-401 has static monthly tie-points. Also, different quality controls is applied in the two products. As a result, OSI-409 could locate icy water surfaces where OSI-401 shows no ice, especially in the Northern hemisphere in boreal summers.

#### 2.6. Screening and pre-processing of input data

The samples from the satellite, in-situ, and ice concentration data sets are trimmed based on the following criteria before ingestion into MUR. In addition, the ice concentration values are used to infer SST values near ice edges.

##### 2.6.1. Quality screening

For the satellite SST retrieval data sets adopting the GHRSSST convention, every SST sample is associated with a quality flag whose value ranges from 0 to 5 in the order of ascending quality. The GHRSSST quality flag generally assesses the level of environmental conditions, such as cloud coverage, known to interfere with satellite SST retrievals. MUR uses only the samples flagged as the highest quality in each data set. The quality flag contained in the non-GHRSSST data sets of OBPG MODIS and Pathfinder is essentially equivalent to the GHRSSST quality flag, and MUR uses the highest quality samples from these data sets also. MUR performs quality screening for the iQuam in-situ data set based on its 16-bit quality flags. MUR uses only the samples flagged to be “high-accuracy”, indicated by the two lowest bits being set to zeros.

The SST samples are compared against a reference SST field, generated during the interpolation procedure ([Section 3.3.3](#)), and those with differences larger than three times the stated or assumed error standard deviation values ([Section 2.6.3](#)) are considered to be outliers and removed from the input data set.

The OSI SAF sea ice concentration data set also contains a quality index (“confidence level”) that ranges from 0 to 5 in ascending order of quality. Again, MUR uses only the samples flagged as the highest quality. In addition, the precision of passive microwave sea ice concentration data has been determined to be on the order of 0.1 in comparison to weekly ice charts, with higher uncertainty for lower concentration values and general difficulty estimating values below 0.1 ([Andersen et al., 2006](#)). MUR thus discards the ice concentration samples valued below 0.1, effectively regarding the locations with ice concentration values below 0.1 to be “ice free”.

##### 2.6.2. Night time samples

Satellite SST retrieval data sets report the skin or sub-skin temperatures ([Donlon et al., 2007](#)) that can vary more than 5°C due to diurnal solar heating. MUR seeks to estimate SST free of such diurnal variation. To reduce the effects of the solar heating, MUR ingests only the SST samples measured between sunset and sunrise in local time. The night-time filter is applied only to the satellite retrieval data sets and not to the in-situ or ice concentration data sets. The combined effect of using only the highest quality samples measured only at night is that roughly 80% of samples in each retrieval data set is discarded before ingestion by MUR on average.

Since moderate to high wind could cause turbulent mixing that diminishes the solar warming at the water surface, future versions of MUR may make use of day-time samples coincident with large enough wind speed (e.g., [Donlon et al., 2012](#)). Since the bulk temperature (at depth) can also display diurnal variation of 0.2 to 0.5°C due to solar heating ([Kawai and Wada, 2007](#)), ingestion of day time samples could still introduce small level of warm bias in a daily SST analysis. The in-situ data can reflect such diurnal variations (up to 0.2°C in drifting buoy data; [Morak-Bozzo et al., 2016](#)). The current version of MUR defers such day-time warming issues by using only the night-time satellite data.

##### 2.6.3. Sensor bias and uncertainty estimates

The GHRSSST convention for SST retrieval data requires each SST sample to be accompanied by single sensor error statistics (SSES) consisting of the *SSES bias* and *SSES standard deviation*. The SSES bias is a statistically inferred difference between the retrieved and in-situ SST values. In principle, since the SST retrieval reports a temperature value at or near the air-sea interface (“skin”), subtraction of the SSES bias



value from the retrieved SST value should yield, on average, a better estimate of the bulk temperature targeted by MUR. For the GHRSSST input data sets, MUR subtracts the SSES bias from each SST sample value before ingestion.

In the non-GHRSSST data sets of OBPB MODIS and Pathfinder, equivalents of SSES bias and SSES standard deviation are absent. The bias for each of these data sets (night-time samples) is assumed to be a constant:  $-0.17^{\circ}\text{C}$  for OBPB MODIS to represent the global average difference between skin and bulk temperature (Donlon et al., 2002), and  $0^{\circ}\text{C}$  for Pathfinder whose SST values are more closely tuned to bulk temperature (Kilpatrick et al., 2001, see also Table 3). In addition, MUR performs inter-sensor bias correction for every data set (Section 3.3.2) to address large-scale bias potentially remaining in the satellite retrievals (Merchant et al., 2009).

The SSES standard deviation  $\sigma$  yields a formal measure of uncertainty in each SST retrieval value in the GHRSSST data sets. For the OBPB MODIS data sets which lack such uncertainty estimates, a constant value of  $\sigma = 0.35\text{K}$  is assumed for all samples, noting that only the samples flagged as “highest quality” are used by MUR. Similarly, a value of  $\sigma = 0.50\text{K}$  is assumed for all samples in the Pathfinder data sets. For the iQuam in-situ data set which also lacks uncertainty estimates, a constant value of  $\sigma = 0.20\text{K}$  is assumed.

#### 2.6.4. SST near ice edges

In SST analysis products, the SST values near sea ice are commonly estimated using empirical relationships between SST and ice concentration. Various regression formulas have been used to relate SST with ice concentration, including a constant (Reynolds and Smith, 1994), linear regression (Reynolds et al., 2007; Donlon et al., 2012), and fits to quadratic (Reynolds et al., 2002; Rayner et al., 2003) and cubic (Hurrell et al., 2008) polynomials. Typically, the SST value is set to a minimum constant temperature ( $-1.8^{\circ}\text{C}$  for the sea,  $0.0^{\circ}\text{C}$  for large lakes) when the ice concentration is above a certain threshold value. When the ice concentration is less than the threshold value, the regression formula is then used to estimate a higher SST value since summer-time SST near sea ice can be several degrees higher than freezing when there is high insolation and light winds. The regression formulas, however, tend to be dependent on the season and region as well as the geographical location within an ocean basin (Rayner et al., 2003).

MUR uses a constant minimum temperature to estimate the ice-edge SST value  $T_{ice}$  when the ice concentration  $F$  is above 0.3 in area fraction. In addition, MUR assumes  $T_{ice} = -1.8^{\circ}\text{C}$  for  $|\phi| > 88^{\circ}$  where  $\phi$  is the latitude, regardless of ice concentration observations. Such a fixed “ice cap” is intended to compensate for relative lack of data near the North Pole.

The uncertainty standard deviation  $\sigma_{ice}$  associated with each  $T_{ice}$  is determined from a scaled version of the cubic polynomial by Hurrell et al. (2008) that approximates the spread of measured SST values as a function of  $F$ . Specifically, Hurrell's polynomial is translated and scaled as  $\sigma_{ice} = 0.5 + 2.057 \times (0.729 - F^3)$  in Celsius for  $F \leq 0.9$  and  $\sigma_{ice} = 0.5^{\circ}\text{C}$  for  $F > 0.9$ . By design, this formula tends to a relatively large uncertainty  $\sigma_{ice} = 2.0^{\circ}\text{C}$  as the ice disappears  $F = 0$ . The aim is to reduce the importance of the assumed ice-edge SST value where actual measurements of SST do exist.

#### 2.7. Use of background SST field

A “background” or “first-guess” field is commonly used in data analysis for a couple of purposes: It could be an integral part of the interpolation procedure, especially as the prior estimate in a Bayesian scheme like the objective interpolation (OI). It could also serve as the reference field with which the outliers in the measurement data sets are determined. Typical sources of the background fields are the most recent analysis (e.g., previous day's analysis in a daily SST analysis product) and a climatological data set. If the background field is a part of

the interpolation procedure, it could be the primary determinant of the analyzed SST values in regions such as polar or cloudy coastal areas where other data are systematically absent for extended periods, and it should hence be considered as an input data set.

The MUR SST analysis uses no background field. The satellite and in-situ SST measurement samples, along with the GHRSSST SST bias estimates (Section 2.6.3) and high-latitude SST values inferred from ice concentration (Section 2.6.4), are the only sources of SST values ingested by MUR.

The MRVA interpolation method used by MUR does not require a prior estimate. For outlier detection, a low-resolution preliminary analysis is created from the same collection of data sets to form a reference SST field (Section 3.3.3). Having such a self-reliant field as the reference is a potential source of bias in the outlier detection procedure. A use of external data such as a climatological data set for the outlier detection procedure is thus under consideration for future versions of MUR. Use of a climatological reference could introduce some risk of rejecting a real, large-magnitude anomalous event (e.g., the Arctic warming of 2007 summer; Steele et al., 2010). Still, an objective approach independent from any external data set, such as a bootstrapping or cross-validation method, would be computationally impractical due to sheer volume of the input.

### 3. Data fusion and interpolation method

Measurement samples are collected over an analysis window of 5 days for each satellite SST data set, while 7-day and 1-day analysis windows are used respectively for the in-situ and ice concentration data sets (Table 1). These windows are centered about the analysis date. Each input data set is expected to supply the temperature  $T$ , the measurement uncertainty standard deviation  $\sigma$ , the geolocation coordinates  $(x, y)$ , and the sampling time  $\Delta t$  relative to the analysis time which is 09:00 UTC of the analysis date. An input data set is denoted as

$$(T_n, \sigma_n, x_n, y_n, \Delta t_n), \quad n = 1, \dots, N \quad (1)$$

where  $N$  is the number of samples from a particular sensor and  $n$  is the sample index. Several such data sets (Fig. 1 and Table 1) are combined using MRVA, a meshless multi-scale interpolation method, to form the daily MUR SST analysis.

The interpolation method needs to be adaptable to the highly variable size of data voids, due to irregular spatial coverages by the satellite orbits and drifter tracks, land interference affecting microwave retrievals near shores, and cloud covers from various weather systems that block infra-red retrievals. The interpolation method must also be able to distinguish the inherent resolution in each data set, from the 1-km scale features resolvable in MODIS retrievals to in-situ SST samples that could be several 100-km apart from each other.

The MRVA method performs a weighted least-squares optimization similar to the objective interpolation (OI) used commonly in SST analysis products, except that MRVA first transforms the input data into additive components based on the spatial scale before data-fusion is performed independently for each of these scale components. Multiple characteristic length scales can be specified in MRVA for interpolation. The longest of these can be selected arbitrarily to smoothly interpolate over the largest of the data voids. The MUR SST analysis uses a scale of approximately 1250 km for the lowest-resolution baseline analysis (Table 2). To address the diversity in the inherent sensor resolution, MRVA controls the highest resolution that each input data set can participate into the scale-dependent component analysis. For example, while the 1-km resolution MODIS data sets are ingested by every analysis component, the 25-km resolution microwave data sets are excluded from analysis components with length-scales finer than approximately 30 km (Tables 1 and 2).

Furthermore, the analysis window for each scale component is varied so that the time window becomes shorter with the resolution of the analysis. This is intended to address the faster evolution speeds

**Table 2**

Scale length and grid dimensions for each scale  $\ell$  used in the MRVA method for the MUR SST analysis. The scale length in km denotes an approximate equatorial distance.

Scale index ( $\ell$ )	Scale length ( $\Delta_\ell$ )		Wavelet grid dimensions	Synoptic window ( $\tau_\ell$ )
	Degrees	km		
0	11.25	1250	$32 \times 16$	48 h
1	5.625	625	$64 \times 32$	48 h
2	2.812	312	$128 \times 64$	48 h
3	1.406	156	$256 \times 128$	48 h
4	0.703	78.2	$512 \times 256$	48 h
5	0.352	39.1	$1024 \times 512$	42 h
6	0.176	19.5	$2048 \times 1024$	36 h
7	0.088	9.77	$4096 \times 2048$	30 h
8	0.044	4.89	$8192 \times 4096$	24 h
9	0.022	2.44	$16384 \times 8192$	18 h
10	0.011	1.22	$32768 \times 16384$	12 h

**Table 3**

Residual statistics for the input data sets of MUR SST analysis: the mean (“bias”), standard deviation (“scatter”), and root-mean-squares (“RMS”) over the global surface. The unit is Celsius. Time-average from years 2002 through 2013 are shown, with the standard deviations (the values after “ $\pm$ ”) representing variability over time.

Data set	Bias	Scatter	RMS
MODIS Terra (OBPG)	$-0.027 \pm 0.070$	$0.474 \pm 0.082$	$0.519 \pm 0.075$
MODIS Aqua (OBPG)	$-0.011 \pm 0.059$	$0.477 \pm 0.089$	$0.515 \pm 0.084$
MODIS Terra (JPL)	$-0.037 \pm 0.051$	$0.398 \pm 0.032$	$0.403 \pm 0.035$
MODIS Aqua (JPL)	$0.029 \pm 0.051$	$0.404 \pm 0.034$	$0.408 \pm 0.034$
Pathfinder Night	$-0.030 \pm 0.104$	$0.607 \pm 0.097$	$0.648 \pm 0.090$
Pathfinder Day	$-0.109 \pm 0.076$	$0.562 \pm 0.120$	$0.634 \pm 0.108$
AVHRR NOAA-18 GAC	$0.035 \pm 0.042$	$0.318 \pm 0.029$	$0.322 \pm 0.034$
AVHRR NOAA-19 GAC	$0.021 \pm 0.037$	$0.310 \pm 0.022$	$0.313 \pm 0.025$
AVHRR MetOp-A GAC	$0.056 \pm 0.040$	$0.261 \pm 0.012$	$0.269 \pm 0.018$
Microwave AMSR-E	$0.019 \pm 0.043$	$0.452 \pm 0.025$	$0.455 \pm 0.026$
Microwave WindSat	$-0.065 \pm 0.093$	$0.568 \pm 0.031$	$0.579 \pm 0.034$
In-situ iQuam	$-0.003 \pm 0.020$	$0.489 \pm 0.046$	$0.489 \pm 0.047$

often displayed by smaller SST features and is achieved by introducing time-dependence to the weight assigned to each data sample. The data weight is typically proportional to the inverse of the uncertainty variance  $\sigma_n^2$ . In MRVA, the weight is further discounted by a decaying function of the sample latency time  $|\Delta t_n|$ . The function decays faster for the smaller analysis scales to achieve the desired effects on the synoptic time scale. For example, the highest-resolution analysis-component uses a rapidly decaying weight resulting in a tight data window of several hours, while the lowest-resolution analysis-component uses a much longer 5-day synoptic window.

Finally, being a “meshless” interpolation technique, MRVA can ingest the geolocation data  $(x_n, y_n)$  directly without approximating them to the locations of the nearest grid points, reducing distortion of the observed features (Chin et al., 2014). A nearest-neighbor approximation is commonly practiced to translate the samples onto the target grid but would truncate the sub-grid coordinates of the geolocation data. MRVA avoids such truncation of geolocation coordinates.

### 3.1. The MRVA interpolation method

The theoretical foundation of MRVA is the *multiresolution analysis* (MRA) which is a signal transformation procedure based on the “scale” (Mallat, 1989; Daubechies, 1992), analogous to the Fourier transform which expands a signal based on the frequency. The notion of “scale” in MRA is similar to the wavelength in Fourier transform; however, the wavelet scales have local extents, which allow the wavelet coefficients to be specific to both the scale and location of signal features, while the Fourier coefficients cannot specify a location unambiguously. Because the scale and location can be adapted separately to the spatial feature, the MRA-based algorithms are intrinsically insensitive to spectral distortion (Alparone et al., 2015). While the sinusoidal functions are the

basis for the Fourier transform, MRA uses orthonormal wavelet functions as the basis for its transform. As in the discrete Fourier transform, the MRA transform is energy conserving and is reversible; the original signal can be reconstructed exactly from the wavelet coefficients.

Standard Fourier transform procedures such as the Fast Fourier Transform algorithm assume that the signal is sampled regularly. For irregularly sampled data, Fourier coefficients can be computed by fitting the sinusoidal functions (Press and Rybicki, 1989). Likewise, the standard MRA algorithm is built on a regularly sampled signal. In order to apply MRA to the irregularly sampled data sets, a variational formulation is used to compute the wavelet coefficients by fitting the wavelet basis to the data. The resulting algorithm is the MRVA method.

Mathematical background and computational details of the MRVA method have been presented by Chin et al. (1998). A review of the MRVA method is presented here, followed by description of additional developments (Section 3.2) introduced for the MUR SST analysis.

#### 3.1.1. Multi-resolution analysis

The resolving power of the wavelet basis is determined by the length scale. The length scale in MRA is normally defined as

$$\Delta_\ell = 2^{-\ell} \Delta_0 \quad (2)$$

for a given scale index  $\ell$  and baseline scale length  $\Delta_0$ . In the MUR SST analysis, we set the baseline length  $\Delta_0 = 360^\circ/2^5 = 11.25^\circ$  in order to: divide the globe evenly along the longitude, facilitate interpolation of the coarsest data set, and set the scale for inter-sensor bias correction.

Consider a two-dimensional function  $T(x, y)$  representing the SST and approximating it using a smooth function  $\bar{T}^\ell(x, y)$ , where the superscript  $\ell$  is the scale index indicating the characteristic length scale  $\Delta_\ell$  that controls the smoothness. As  $\ell$  increases, the resolution of the analysis  $\bar{T}^\ell(x, y)$  increases. The MRA transformation expands the signal into a single low-resolution baseline mean field  $\bar{T}^0(x, y)$  plus a hierarchy of variability fields  $\hat{T}^\ell$ , each defined by the one-step finer length scale  $\Delta_{\ell+1}$ , that capture increasingly high-resolution details. We use  $\hat{T}_0^L(x, y)$  to denote the expansion as

$$\hat{T}_0^L(x, y) = \bar{T}^0(x, y) + \sum_{\ell=0}^{L-1} \hat{T}^\ell(x, y) \quad (3)$$

where the subscript 0 indicates the resolution of the baseline analysis and the superscript  $L$  indicates the number of the variability fields as well as the scale  $\Delta_L$  of the highest resolvable features in the analysis  $\hat{T}_0^L(x, y)$ . In principle, the number  $L$  of the variability fields needs to be infinite to represent a continuous signal exactly or  $T(x, y) = \hat{T}_0^\infty(x, y)$ ; however, in practice the signal will be bandlimited by the numerical grid that represents it, and hence  $L$  is a finite number. In particular, a value of  $L = 10$  would be sufficient for a  $0.01^\circ \times 0.01^\circ$  grid (Table 2).

When applied to an interpolation problem, the approximation function  $\bar{T}^\ell$  would not be well defined over a data void several times larger than the characteristic length scale  $\Delta_\ell$ . On the other hand, the variability function  $\hat{T}^\ell$  could reasonably be assumed to be zero (or to have zero mean, Chin et al., 1998) in the middle of the same data void. It is thus possible to have  $\hat{T}^\ell \neq \bar{T}^{\ell+1} - \bar{T}^\ell$ , and hence  $\hat{T}_0^L \neq \bar{T}^L$ , when the multi-scale decomposition (3) is applied to interpolation. A key advantage of the multi-scale analysis  $\hat{T}_0^L$  is that the scale of the baseline analysis can be chosen arbitrarily long to interpolate over the largest data voids without compromising the highest resolvable features and without introducing large spurious features over the data voids. Either of these can be achieved using a single-scale analysis  $\bar{T}^\ell$ , but not both. Fig. 2 demonstrates such distinctions. In particular, when a large enough data void is present (center rectangle, top-left panel, Fig. 2), a single-scale high-resolution interpolation could introduce significant artifacts in the area of the void (bottom-left panel), while a multi-scale interpolation can suppress such artifacts by design (top-right panel) which fills the void with a low-resolution version (bottom-right panel).

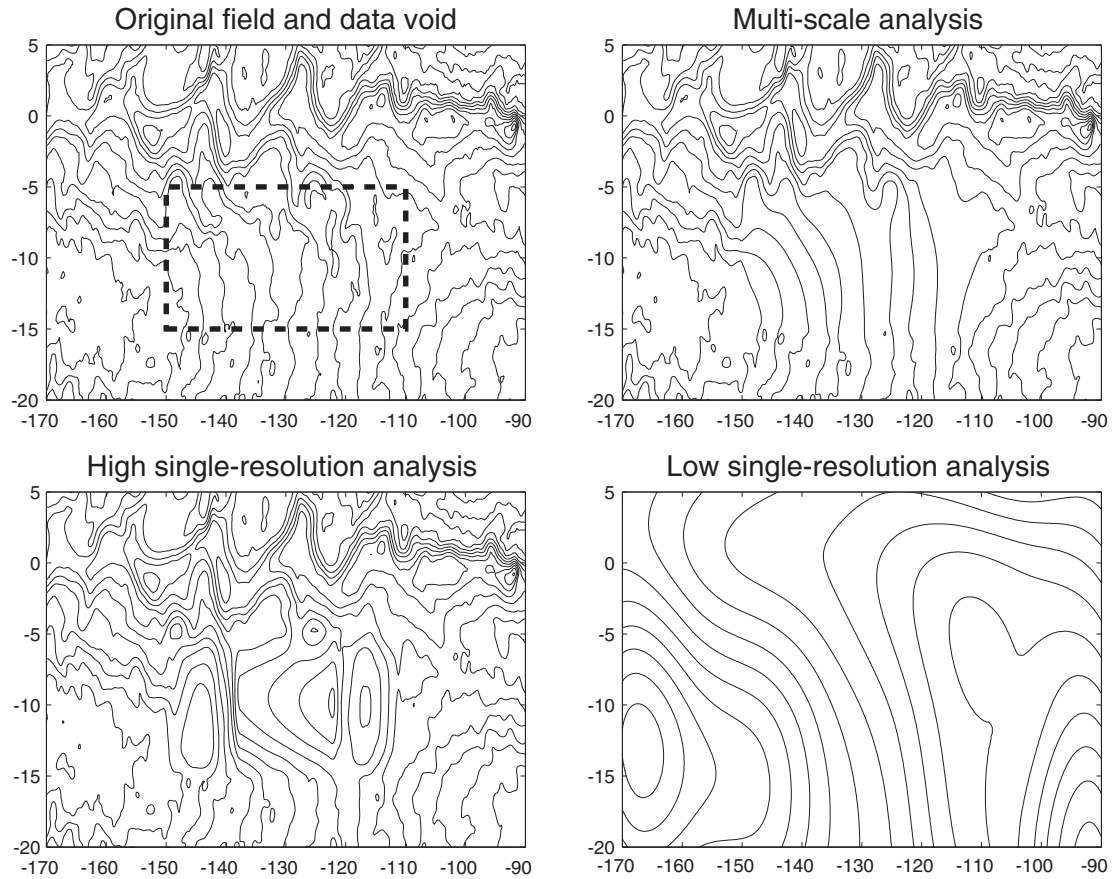


Fig. 2. A demonstration of multi-scale analysis using the MRVA method. Top-left: an SST field from which data are sampled every  $0.2^\circ$  in longitude and latitude except inside the rectangular box (dashed line) representing a large data void. Top-right: multi-scale interpolation  $\hat{T}_0^6$  of the sampled data. Bottom-left: a single-scale high-resolution interpolation  $\bar{T}^6$ , which produces spurious features in the area of the data void. Bottom-right: a single-scale low-resolution interpolation  $T^0$ , which is also identical to the baseline analysis contained in the multi-scale  $\hat{T}_0^6$ .

### 3.1.2. Wavelet basis functions

Each of the additive components in the expansion (3) is itself an expansion with the wavelet basis functions. In MRA, the basis  $\phi$  for the mean fields  $\bar{T}^\ell$  is called the *scaling function* (or *father wavelet*), and the basis  $\psi$  for the variability fields  $T^\ell$  is called the *wavelet function* (or *mother wavelet*). MRA is a loss-less and reversible transform since the wavelet functions ( $\phi, \psi$ ) form a mutually orthonormal basis over the space ( $x, y$ ) and across the scale  $\ell$  (Daubechies, 1992).

Unlike the Fourier transform, MRA has more than a single choice for its basis function. Fig. 3a shows the third-order (cubic) Battle-Lemarié wavelet basis (Battle, 1987; Lemarié, 1988) used in the MRVA method and MUR analysis. Both basis functions effectively have local extents, in

contrast to the global extent of the sine and cosine functions that form the basis for the Fourier transform. The Battle-Lemarié wavelet basis is a “spline wavelet” (Chui and Wang, 1991; Unser, 1997) which possesses desirable properties including differentiability, symmetry, optimal space-wavenumber localization, and fastest rates of decay in approximation error among the known wavelet transforms (Unser, 1997).

The frequency-response of the cubic Battle-Lemarié wavelet transform, shown in Fig. 3b, implies that the scale length  $\Delta_\ell$  is roughly equal to the Nyquist sampling interval. The length scale of an analysis can thus approximate the smallest *wavelength* featured in the analysis. In general, the variability fields are effectively bandpass filtered versions of the signal, while the baseline mean field is a low-pass filtered

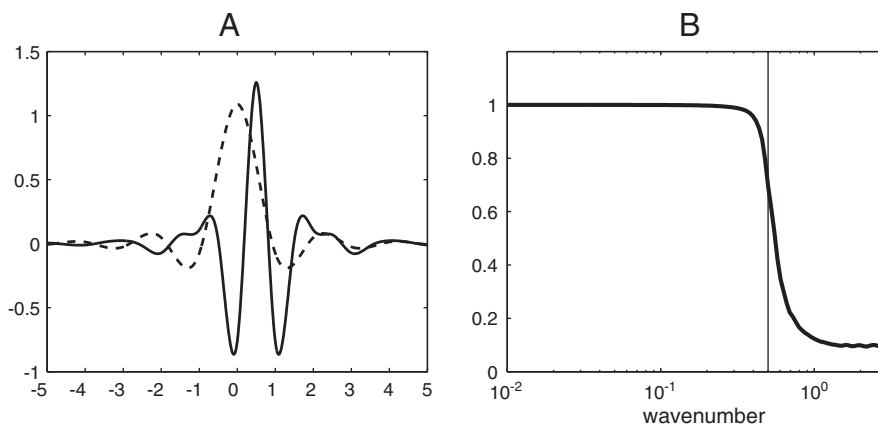


Fig. 3. Cubic Battle-Lemarié wavelet analysis. [a] The basis generating functions  $\phi$  (dashed line) and  $\psi$  (solid line): Note that the scaling function  $\phi$  is shaped to determine a local average when convolved, while the wavelet function  $\psi$  is shaped to sample a local difference. [b] Transfer function of a stage of MRVA interpolation when the scale parameter is a unit distance ( $\Delta_\ell = 1$ ), corresponding to a sampling rate of 1 per unit distance: The vertical line indicates the Nyquist maximum wavenumber (signal bandwidth) of  $1/2$  for this sampling rate. While MRVA is not a perfect low-pass filter, the cut-off wavenumber approximates the Nyquist bandwidth well, implying that the wavelet scale ( $\Delta_\ell$ ) approximates the Fourier wavelength at the Nyquist limit.

version. These variability bands cover the wavenumber spectrum without overlapping with each other because the set of scale lengths is specified exactly (Wornell, 1993), as in Eq. (2).

### 3.1.3. Wavelet coefficients

Two-dimensional wavelet basis functions are obtained by a tensor product of the one-dimensional versions, analogous to the way two-dimensional Fourier basis is constructed. Using the two-dimensional basis, the “mean” and “variability” components of the signal are each expanded in terms of the wavelet coefficients  $C_{ij}^\ell$ ,  $D_{ij}^\ell$ ,  $E_{ij}^\ell$ , and  $F_{ij}^\ell$  as

$$\bar{T}^\ell(x, y) = \sum_{(i,j)} C_{ij}^\ell \cdot \phi(x/\Delta_\ell - i) \cdot \phi(y/\Delta_\ell - j) \cdot 2^\ell \quad (4)$$

$$\begin{aligned} \dot{T}^\ell(x, y) = & \sum_{(i,j)} D_{ij}^\ell \cdot \psi(x/\Delta_\ell - i) \cdot \psi(y/\Delta_\ell - j) \cdot 2^\ell \\ & + E_{ij}^\ell \cdot \psi(x/\Delta_\ell - i) \cdot \phi(y/\Delta_\ell - j) \cdot 2^\ell \\ & + F_{ij}^\ell \cdot \phi(x/\Delta_\ell - i) \cdot \psi(y/\Delta_\ell - j) \cdot 2^\ell \end{aligned} \quad (5)$$

where  $i$  and  $j$  are location coordinate indices (Chin et al., 1998). The wavelet basis controls its scale by modulating its spatial extent by the given characteristic length  $\Delta_\ell$  and its location by translating its center by the location indices  $(i, j)$ . With the normalization constant  $2^\ell$  all basis functions are dimensionless, so that the coefficients have the physical unit of the signal (e.g. temperature).

The dimension of the coefficient grid  $(i, j)$  for the global surface coverage is  $(360^\circ/\Delta_\ell) \times (180^\circ/\Delta_\ell)$  and is tabulated for each  $\ell$  in Table 2. By design, the number of grid points increases by fourfold with each increment in the scale  $\ell$ . Since each grid point is associated with a wavelet coefficient, the total number of all four types of coefficients ( $C_{ij}^\ell$ ,  $D_{ij}^\ell$ ,  $E_{ij}^\ell$ , and  $F_{ij}^\ell$ ) in  $\hat{T}_{\ell-1}^\ell$  is the same as the number of coefficients in  $\bar{T}^\ell$ . By induction, therefore, the total number coefficients in the multi-scale representation  $\hat{T}_0^L$  is identical to the number of coefficients in the single-scale analysis  $\bar{T}^L$ . This efficiency in the multi-scale representation is a benefit of using the MRA transformation.

### 3.1.4. Variational formulation

Since the MRA basis functions are mutually orthonormal, the wavelet coefficients can be computed using a straightforward inner product between the signal and the basis function (e.g., Chin et al., 1998),

$$C_{ij}^\ell = \frac{1}{\Delta_0^2} \iint_{\mathcal{S}} T(x, y) \cdot \phi(x/\Delta_\ell - i) \cdot \phi(y/\Delta_\ell - j) \cdot 2^\ell \, dx \, dy, \quad (6)$$

and an analogous formula for each of  $D_{ij}^\ell$ ,  $E_{ij}^\ell$ , and  $F_{ij}^\ell$ , where  $\mathcal{S}$  is the spatial domain (global ocean surface). Numerical computation of the integrals, however, usually requires a fully and uniformly gridded signal  $T(x, y)$  to be practical. The satellite and in-situ SST data at hand are rarely sampled densely and uniformly enough to approximate the integrals accurately.

Alternatively, an optimization formula is used to fit the basis functions to the given data to compute the coefficients. A least-squares formula has been used to perform Fourier transform for irregularly sampled signals (Press and Rybicki, 1989), and a similar approach is taken in MRVA. To fit a two-dimensional function  $T(x, y)$  to a given data set (1), the analysis residual function

$$\mathcal{S}(T) \equiv \sum_{n=1}^N w_n [T(x_n, y_n) - T_n]^2 \quad (7)$$

is minimized with respect to the wavelet coefficients. The data weight  $w_n$  is usually specified by the measurement uncertainty as  $\sigma_n^{-2}$  but is further modified according to the analysis scale  $\ell$  and data density as described in Section 3.2. Because of the highly irregular distribution of the data over the space  $\mathcal{S}$ , the minimization problem is regularized using the standard thin-plate model (Inoue, 1986; Bookstein, 1989)

$$\begin{aligned} \mathcal{R}(T) \equiv & \tilde{w}^{10} \left( \frac{\partial T}{\partial x} \right)^2 + \tilde{w}^{01} \left( \frac{\partial T}{\partial y} \right)^2 + \tilde{w}^{20} \left( \frac{\partial^2 T}{\partial x^2} \right)^2 + \tilde{w}^{02} \left( \frac{\partial^2 T}{\partial y^2} \right)^2 \\ & + \tilde{w}^{11} \left( \frac{\partial^2 T}{\partial x \partial y} \right)^2. \end{aligned} \quad (8)$$

The regularization weights  $\tilde{w}$  can be specified to represent flow-dependent correlation patterns (Fig. 3 in Chin et al., 2014). For the MUR SST analysis, however, isotropic correlation structure is used due to the generally high data density (Section 3.3.3). MRVA minimizes the regularized data-residual function

$$\min \iint_{\mathcal{S}} \mathcal{R}(\hat{T}_0^L) + \mathcal{S}(\hat{T}_0^L) \, dx \, dy \quad (9)$$

with respect to the coefficients  $C_{ij}^\ell$ ,  $D_{ij}^\ell$ ,  $E_{ij}^\ell$ , and  $F_{ij}^\ell$  for  $\ell = 0, \dots, L-1$ . Solution for these coefficients involves inversion of a linear system of normal equations as detailed by Chin et al. (1998).

### 3.2. Data weight

The weight  $w_n$  in the data residual function (7) controls the importance of each data sample  $T_n$  to the analysis. The inverse variance  $\sigma_n^{-2}$  is used commonly as the data weight; however, such a practice ignores the cross-correlation among the nearby samples with undesirable consequences including unrealistically small error estimates (Kaplan et al., 2003). Additionally, in multi-scale analysis, the importance of samples with large latency time  $|\Delta t_n|$  decreases as the analysis scale  $\ell$  becomes finer. To address these issues, the data weight in MUR is given as

$$w_n = \gamma_n \cdot \delta_n^\ell \cdot \sigma_n^{-2} \quad (10)$$

where  $\gamma_n$  and  $\delta_n^\ell$  are dimensionless discount factors that represent the effects of cross-correlation and data-latency, respectively, as detailed in this section.

#### 3.2.1. Intra-bin correlation

Uneven spatial distribution of highly concentrated samples, such as those exhibited by the MODIS data sets, can lead to spurious analysis features due to unfavorable numerical condition in the inversion procedure if the data are assumed to be mutually independent, as demonstrated by Chin et al. (2014) who also suggest a simple solution using a “fictitious correlation coefficient”  $\rho$ . MUR adopts such a solution and defines the correlation discount factor as

$$\gamma_n = \frac{1}{1 + \rho(\Lambda_n - 1)} \quad (11)$$

where  $\Lambda_n$  is the number of samples in the wavelet grid-box that contains  $(x_n, y_n)$ . The given correlation coefficient  $\rho$  is assumed to be constant between any two samples from the same data set in the same grid-box. The formulation (11) has plausible asymptotic properties that  $\gamma_n$  tends to  $\Lambda_n^{-1}$  (simple average of the weights) as  $\rho$  approaches one,  $\gamma_n$  tends to one (no discount) as  $\rho$  approaches zero, and  $\gamma_n$  tends to  $\Lambda_n^{-1} \rho^{-1}$  (an inflated average of the weights) as the data density  $\Lambda_n$  increases (see Chin et al., 2014).

In multi-scale interpolation of the SST data sets, the spatial distribution of the samples nominally becomes more uniform as the grid-box enlarges. MUR thus uses an assumed correlation  $\rho$  that decreases with the length scale  $\Delta_\ell$  of the analysis component as  $\rho = 0.8 \cdot \exp(-\Delta_\ell/4^\circ)$  which specifies a negligible correlation ( $\rho = 0.0$ ) for the baseline component ( $\ell = 0$ ) but increases quickly and saturates to a value between 0.7 and 0.8 for the higher-resolution analysis components ( $\ell \geq 5$ ).

#### 3.2.2. Time-windowing

In the MUR SST analysis, the length of “synoptic” window varies with the resolution of the multi-scale analysis-component. The MRVA interpolation method achieves this through the discount factor



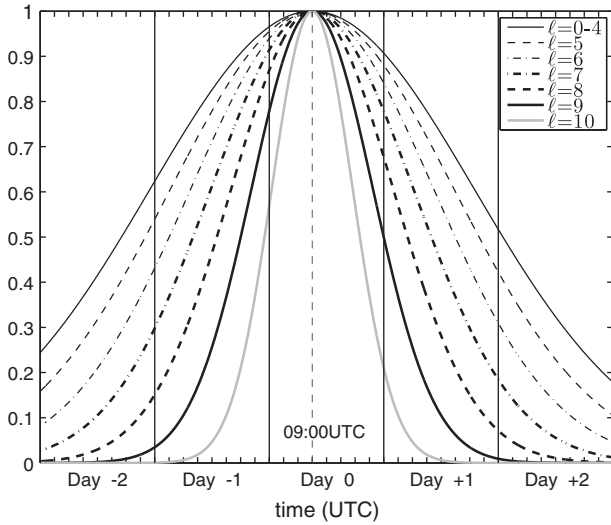


Fig. 4. The synoptic discount factor  $\delta_n^\ell$  as a function of the analysis resolution  $\ell$ . The width of the synoptic window narrows as the analysis resolution  $\ell$  increases.

$$\delta_n^\ell = \exp[-(\Delta t_n/\tau_\ell)^2] \quad (12)$$

where  $\tau_\ell$  is the scale-dependent window duration, which ranges from 12 to 48 h in the current version of MUR as given in Table 2. The corresponding discount factors  $\delta_n^\ell$ , shown in Fig. 4 over a 5-day window for different resolutions  $\ell$ , indicate narrower windows for finer resolutions.

The scale-varying window duration is critical to fidelity of high-resolution analysis. Fig. 5 demonstrates that, if a constant window ( $\tau_\ell = 960$  hours for all resolutions  $\ell$ ) is used, inclusion of higher-resolution components could actually increase the analysis error (dashed line for  $6 \leq L \leq 9$ ) because the small scale features evolve significantly during the window period. The period is too long for a synoptic perspective at such small scales, and the higher resolution components are effectively adding noise (increasing error on average) to the final analysis. Such an undesirable effect can be mitigated by use of the window duration  $\tau_\ell$  that decreases with the resolution  $\ell$  (Table 2, Fig. 4), in

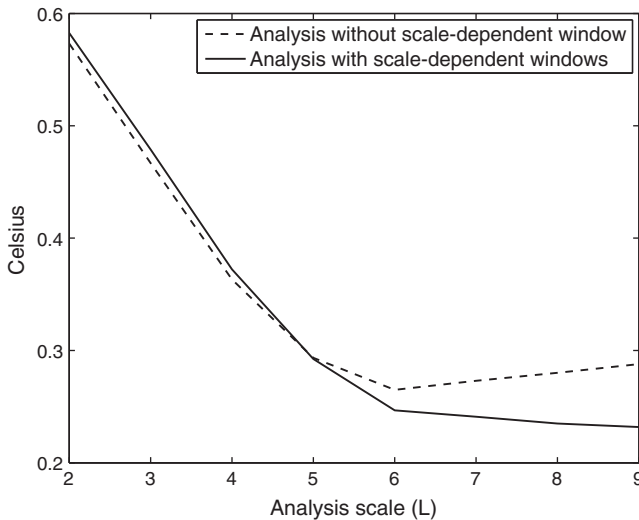


Fig. 5. Analysis error of MRVA as a function of the analysis resolution  $L$ , using the synoptic window  $\delta_n^\ell$ , with (solid line) and without (dashed line) a scale-dependent duration (see text). In both cases, simulated SST from a  $1/48^\circ$ -resolution ECCO2 ocean circulation model (Menemenlis et al., 2008) is used, where an hourly sequence during December 2011 is sampled at the coincident MODIS Terra, MODIS Aqua, and WindSat sampling locations to form the input data sets. The analyzed SST fields are compared to the coincident ECCO2 SST fields to determine the analysis error as a root-mean-squares global average.

which case the inclusion of the high resolution components does decrease the overall error (solid line, Fig. 5) as desired.

### 3.3. Data fusion

Because the data weight  $w_n$  is dependent on the analysis scale  $\ell$  as well as the individual data set, MRVA needs to accommodate these dependencies for MUR. MRVA is also used to estimate the inter-sensor bias fields which are removed while combining samples from all data sets. Formulations of these procedures are developed based on the existing MRVA realization.

#### 3.3.1. Scale-dependent analysis residuals

To accommodate the scale-dependent data weight  $w_n$ , the wavelet coefficients are evaluated separately for each  $\ell$ , instead of jointly in a single matrix inversion as implied by Eq. (9). The data weight is also dependent on the data density and hence is distinct for each data set. Moreover, all but the MODIS data sets are excluded from the analysis components for the resolution  $\ell$  higher than the maximum specified for each data set (Table 2), and such exclusion is realized by setting  $w_n = 0$  for the particular data set and  $\ell$ .

To denote dependence on the data set, we will add the data set index  $m$  to the analysis residual function as  $\mathcal{S}_m(T)$  for  $m = 1, \dots, M$  where  $M$  is the number of data sets ingested. The baseline analysis coefficients  $C_{ij}^0$  can then be determined by minimizing

$$\min \iint_{\mathcal{G}} \mathcal{R}(\bar{T}^0) + \sum_{m=1}^M \mathcal{S}_m(\bar{T}^0) dx dy. \quad (13)$$

The variability coefficients  $D_{ij}^\ell$ ,  $E_{ij}^\ell$ , and  $F_{ij}^\ell$  can be determined by subsequent minimizations

$$\min \iint_{\mathcal{G}} \mathcal{R}(\hat{T}^\ell) + \sum_{m=1}^M \mathcal{S}_m^\ell(\hat{T}^\ell) dx dy. \quad (14)$$

based on the scale-dependent analysis residual function

$$\mathcal{S}_m^\ell(T) \equiv \sum_{n=1}^N w_n^\ell [T(x_n, y_n) - \Delta T_n^\ell]^2 \quad (15)$$

where the residual data samples are defined as

$$\Delta T_n^\ell \equiv T_n - \hat{T}_0^\ell(x_n, y_n) \quad (16)$$

iteratively for  $\ell = 0, 1, \dots, L-1$ . Note that by definition  $\Delta T_n^0 = T_n - \bar{T}^0(x_n, y_n)$ .

#### 3.3.2. Inter-sensor bias estimation

MUR must estimate SSES biases for the non-GHRSST satellite data sets that do not provide their own (Section 2.6.3). The SSES bias estimation procedure can also vary among the GHRSST data sets, and analysis artifacts along the edges of satellite swaths can appear due to systematic biases in the data sets relative to each other. MUR thus estimates an additional bias field for every satellite data set.

Inter-sensor bias is assumed to be a smooth field (containing only low-resolution features) since it is mostly indicative of systematic tendencies of sensor retrieval that vary relatively slowly over time. Also, the in-situ data set (iQuam) is assumed to have null bias. Inter-sensor bias correction takes place while simultaneously estimating the baseline analysis  $\bar{T}^0(x, y)$ . Specifically, the bias  $b_m(x, y)$  for the data set  $m$  is represented by the “mean field”

$$\bar{b}_m^\ell(x, y) = \sum_{(i,j)} (B_{ij}^\ell)_m \cdot \phi(x/\Delta_\ell - i) \cdot \phi(y/\Delta_\ell - j) \cdot 2^\ell \quad (17)$$

with the associated wavelet coefficients  $(B_{ij}^\ell)_m$ . The length scale of the bias field is set to be  $\ell = 0$ , and the baseline analysis coefficients  $C_{ij}^0$  and bias field coefficients  $(B_{ij}^0)_m$  are simultaneously determined from the minimization

$$\min \iint_{\mathcal{G}} \mathcal{R}(\bar{T}^0) + \sum_{m=1}^M \mathcal{R}(\bar{b}_m^0) + \mathcal{S}_m(\bar{T}^0 + \bar{b}_m^0) dx dy \quad (18)$$

where  $\bar{b}_m^0 = 0$  if  $m$  is the index for the iQuam data set.

### 3.3.3. The SST analysis

Data fusion in MUR is accomplished by the bias-corrected baseline field estimation from Eq. (18), followed by the variability field estimations from Eq. (14) iteratively for  $\ell = 0, 1, \dots, L - 1$  where the analysis scale  $L$  for the current version of MUR is set to be  $L = 9$ . An analysis scale less than the maximum possible scale ( $L = 10$ ) has been chosen through post-analysis evaluation of the high-resolution components (Sections 4.3 and 4.4). The smoothness of the analysis components has also been determined to be  $\hat{w}^{10} = \hat{w}^{01} = 1.0$ ,  $\hat{w}^{20} = \hat{w}^{02} = 0.2$ ,  $\hat{w}^{11} = 0.4$  (Section 3.1.4).

The set of estimated wavelet coefficients determines the final MRVA estimate  $\hat{T}_0^L(x, y)$  through Eq. (3), which can be sampled anywhere on a continuous global surface. Sampling of  $\hat{T}_0^L(x, y)$  over a  $0.01^\circ \times 0.01^\circ$  grid yields the MUR SST analysis data product.

During each production session for MUR, a separate MRVA estimate  $\hat{T}_0^4(x, y)$  at a lower-resolution is created first for detection of outliers in the input data sets (Section 2.7). The resolution of  $L = 4$  is the highest resolution that includes all input data sets (Table 1). After the outliers are removed from the inputs, the final MRVA field  $\hat{T}_0^9(x, y)$  is then determined.

### 3.4. Auxiliary gridded fields

Each MUR product file contains four auxiliary fields besides the main analysis  $\hat{T}_0^L(x, y)$ , all on the identical  $0.01^\circ \times 0.01^\circ$  grid. Three of the auxiliary fields are common in all GHRSSST “level 4” gridded products and are the *analysis error*, *land mask*, and *ice fraction* fields. The fourth auxiliary field, unique to the MUR product, indicates the latency time to the most recent “1 km data” (MODIS) sample. The latter field, called *high-resolution data latency* field, is intended as a quality indicator for the analyzed high-resolution SST features.

#### 3.4.1. Analysis error field

The standard deviation of the formal estimation error is provided at each grid point as an estimate of analysis uncertainty. The wavelet coefficients are determined from a set of least-squares minimizations, and solution of a least-squares problem involves inversion of a normal equation. In the standard estimation theories, the inverse of the normal equation matrix is the formal estimation-error covariance matrix, whose diagonal elements yield the error variance estimates. Because the wavelet coefficients under the MRVA method have the unit of the physical field (i.e., temperature), the posterior error covariances associated with the estimated coefficients also have a consistent physical unit. MUR thus uses the square-root variances directly as the coefficients for the uncertainty analysis

$$\bar{\sigma}^\ell(x, y) = \sum_{(i,j)} \sqrt{P_{ij}^\ell} \cdot \phi(x/\Delta_\ell - i) \cdot \phi(y/\Delta_\ell - j) \cdot 2^\ell \quad (19)$$

analogous to the expansion (4) of the physical field where  $P_{ij}^\ell$  is the formal posterior error variance associated with the wavelet coefficient  $C_{ij}^\ell$ .

#### 3.4.2. Land mask and ice fraction fields

The sea ice fraction field indicates the areal fraction of surface ice coverage in the vicinity of each grid point. MUR simply projects the input ice concentration data set (Section 2.5) onto the grid to form the ice fraction field. The quality control procedure described previously (Section 2.6.1) is applied to the ice data samples before projection onto the grid.

The land mask field contains flags to indicate whether the grid point

is a part of land, sea, or lake. The Generic Mapping Tools (GMT) software (<http://gmt.soest.hawaii.edu/projects/gmt>) is used to generate such a field. Lakes and islands with areas less than  $10,000 \text{ km}^2$  are flagged as “land” and “sea” respectively to reduce clutter. In addition, the sea and lake grid-points that coincide with non-zero ice fraction values are marked as “icy sea” and “icy lake”.

#### 3.4.3. Latency of the most recent MODIS samples

The high-resolution data latency field, labeled as “dt-1km-data” in the MUR product files since year 2016, simply reports the  $\Delta t_n$  values with the smallest magnitude from either of the MODIS data sets. The latency field can determine quality of small-scale SST features found near a particular grid point. The  $\Delta t_n$  values, the sample times minus the analysis time (09:00 UTC each day), from the MODIS data sets are grouped into  $0.01^\circ \times 0.01^\circ$  bins around each grid point, and the value with the smallest magnitude in each bin is reported in the dt-1km-data field in the unit of hours. If 1-km resolution SST data sets other than the MODIS data (such as the VIIRS data) are to be ingested by MUR in the future, the  $\Delta t_n$  values from such data sets will be included in the dt-1km-data field.

### 3.5. Near real time analysis fields

Since MUR specifies up to seven days of analysis window centered about the analysis date, a complete set of input data would become available only after four days of latency relative to the present time. For the dates less than four days into the past, MUR performs *preliminary analysis* using an incomplete input data set. The preliminary analysis fields are updated every day using additional retrieval and in-situ data that become available, until the fourth update which would become the *final analysis* with the complete input data set.

## 4. Evaluation of the SST analysis

The MUR SST analysis (<http://dx.doi.org/10.5067/GHGMR-4FJ04>) is available as a GHRSSST data product from the Long Term Stewardship and Reanalysis Facility (LTSRF) at NOAA NCEI and the Physical Oceanography Distributed Active Archive Center (PO.DAAC) at NASA JPL. Various visualization tools for MUR are also available (e.g., <http://mur.jpl.nasa.gov/images.php>).

Analyzed SST values are commonly validated through comparison to other data sets. The traditional reference for validation of the bulk SST estimate is derived from the in-situ SST measurements. However, quality control of in-situ SST data is a dedicated task, and the sampling is too sparse in space for comparison of the meso-scale and smaller SST features. In this section, we compare MUR to other gridded SST analysis products to examine the meso-scale patterns as well as the bulk SST values in MUR. Higher-resolution SST features in MUR is then evaluated through comparison to the VIIRS retrieval data, which provide independently derived 1-km scale SST patterns at wide enough spatial coverage but with data voids. Moreover, MUR is compared against its own inputs for examination of data residuals and their scale dependent characteristics in order to evaluate performance of the multi-scale analysis approach used by MUR.

#### 4.1. Data residuals

Contributions of each input data set to the MUR SST fields are examined through statistics of the residual data. The residuals  $T_n - \hat{T}_0^L(x_n, y_n)$  are calculated directly from the wavelet coefficients instead of interpolating the gridded SST values to the sample location  $(x_n, y_n)$ . The data samples  $T_n$  are quality-controlled and preprocessed in the same manner as the analysis inputs (Section 2.6), except that a single-day window is used here for all data sets. In particular, the SSES (or assumed) bias is applied for surface-to-bulk conversion of the SST

values, and the quality flag is used to select only the “highest quality” samples.

#### 4.1.1. Residuals of the MUR inputs

Table 3 lists global statistics of the input residuals for the data ingested by MUR from years 2003 through 2013. The mean residuals (“bias”) are generally small, with magnitudes less than  $0.07^{\circ}\text{C}$  except for the large negative bias in one of the Pathfinder data sets which are known for “cold bias” tendencies (e.g., O’Carroll et al., 2012). The iQuam data set shows the smallest bias as expected, since it serves as the reference in the inter-sensor bias correction by MRVA.

Because of the generally small bias for all input data sets, the root-mean-squares (RMS) residual is dominated by the residual scatter (standard deviation about the mean bias). The smallest RMS residuals, of around  $0.3^{\circ}\text{C}$ , are reported by the AVHRR GAC data sets.

The non-GHRSSST data sets without the SSES bias, namely the OBPB MODIS and Pathfinder data sets used in this version of MUR, have relatively large RMS residuals. The RMS values of the OBPB MODIS data sets are more than  $0.1^{\circ}\text{C}$  higher than their JPL counterparts, while the Pathfinder RMS residuals are more than  $0.3^{\circ}\text{C}$  higher than the RMS values for the AVHRR GAC data. A possible cause for the larger RMS residuals is the constant bulk-SST bias ( $-0.17^{\circ}\text{C}$ ) assumed for the non-GHRSSST data sets, in contrast to the GHRSSST data sets which provide each sample with an individualized SSES bias. The constant bias cannot account for regional and seasonal variability in the skin-to-bulk SST difference, and the unaccounted variability could appear as additional data residual.

A bulk-SST bias individualized for each surface sample would be desirable for the non-GHRSSST retrieval data sets to replace the constant bias. Such replacements have become possible recently. In particular, an updated version of the OBPB MODIS SST data sets now include SSES bias estimates. Also, updated Pathfinder data sets as well as reprocessed AVHRR GAC data sets (Ignatov et al., 2016) have become partially available for the period currently covered by the Pathfinder data in MUR. These new data sets are planned for ingestion by a future version of MUR.

#### 4.1.2. Dependence on analysis scale

The inherent feature resolution  $L$  is a key parameter in the MRVA method. Contribution by each data set to MUR is scale dependent and is controlled by the maximum scale assigned to each data type (Eq. (3) and Table 1). We examine such scale-dependency by computing data residuals for the analyses with varying feature scales. Specifically, data residuals are examined for each of the analysis  $\hat{T}_0^L$ , which we call *siblings* of MUR, for  $L = 1, \dots, 9$ . Note that the setting  $L = 9$  specifies MUR itself.

Fig. 6 shows data residuals as a function of the analysis resolution  $L$ . The RMS residuals for all input data sets except MODIS are found to increase sharply just beyond the maximum ingestion resolution (Table 1) for the particular data set:  $L = 4$  for in-situ,  $L = 6$  for microwave, and  $L = 7$  for AVHRR GAC data types (thin lines with marks). For example, the RMS residual of the in-situ iQuam data set is as low as  $0.32^{\circ}\text{C}$  for a low-resolution sibling ( $L = 4$ ) but increases by at least  $0.15^{\circ}\text{C}$  for the higher-resolution siblings ( $5 \leq L \leq 9$ ). Such a jump in iQuam residual implies that, from the perspective of the in-situ data, any higher-resolution variability originated from other data types would appear as “noise”. The relatively large magnitude of the jump can be attributed to relatively small sample size of the iQuam data set which could be dominated by other data sets with higher spatial densities.

The RMS residual for the MODIS data (thick solid line, Fig. 6) decreases monotonically with the scale, indicating that consistency between MODIS and MUR siblings increases as the analysis resolution  $L$  is raised. In other words, at least some aspects of the SST features represented by the MODIS data sets are captured by MUR for all scales  $L \leq 9$ , implying successful transfer of high resolution SST features from

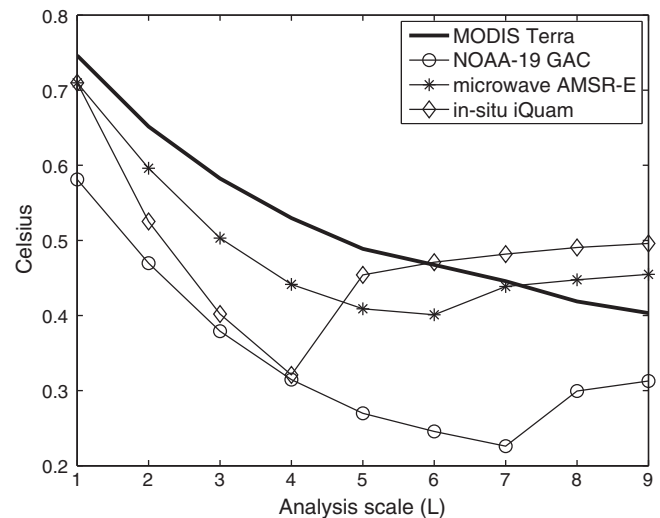


Fig. 6. Root mean squares difference between MUR and its input data sets as a function of the analysis scale  $L$ . A representative from each input data type is selected from Table 3.

the data to analysis. The monotonic decrease in the MODIS residual is an indication that the multi-scale analysis scheme (MRVA) has performed as expected for the high resolution data sets.

#### 4.2. Comparison to gridded SST products

Existing gridded analysis products are convenient for comprehensive comparison of the spatial patterns since they provide bulk SST estimates free of systematic voids. Over a dozen daily global SST analysis products are available in the GHRSSST-formatted collection alone, for a variety of operational, scientific, and recreational uses. Several of these products have established validation history through years of scientific and operational usages as well as comparison to in-situ measurements, and they could provide the baseline SST fields to validate a new analysis approach like the MRVA method used to generate MUR.

Analysis products are hardly independent from each other since most products ingest common inputs such as the AVHRR and in-situ data. However, difference among the analyzed SST fields can still be significant due to differences in quality control and interpolation procedures (Dash et al., 2010, 2012). When several SST analyses are projected onto a common grid, ensemble statistics such as the mean, median, and standard deviation can be determined at each grid point. A field of median SST values from an ensemble of approximately ten operational daily SST analysis products is provided by the GHRSSST Multi-product Ensemble (GMPE) project (Martin et al., 2012) which reports that the GMPE analysis shows better agreements with in-situ SST measurements than any of the individual products in the GMPE membership.

The GMPE median SST analysis is compared to MUR as well as three GMPE member products. The three products are the *Optimum Interpolation SST* analysis from NCEI (Reynolds et al., 2007), *CMC SST analysis* from the Canadian Meteorological Centre (Brasnett, 2008), and *Operational Sea Surface Temperature and Sea Ice Analysis (OSTIA)* from the UK Met Office (Donlon et al., 2012). Fig. 7 shows the RMS differences between GMPE and each of the four products over a four-year period. MUR (dark thick line) agrees with GMPE at a similar level as the three member products (thin lines with marks) even though MUR is not a member of GMPE.

Fig. 7 also shows the RMS difference between GMPE and a low-resolution sibling  $\hat{T}_0^6$  of MUR (dashed line). The low-resolution sibling agrees with GMPE better than MUR itself because it has a similar resolution as GMPE which uses a  $0.25^{\circ} \times 0.25^{\circ}$  grid. The RMS difference

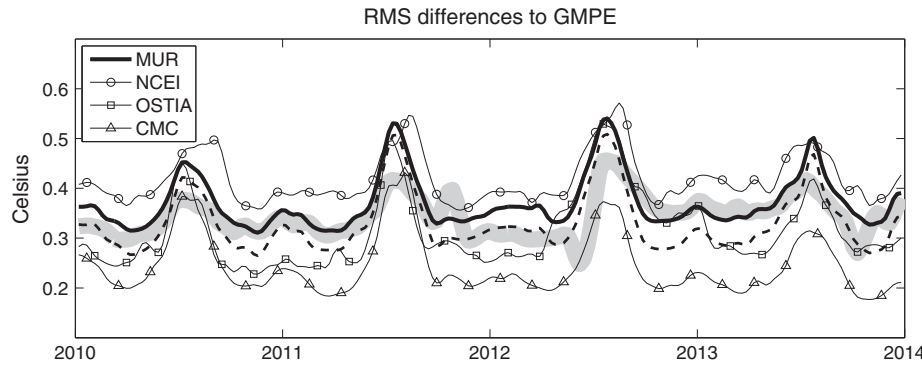


**Fig. 7.** Global root mean squares (RMS) difference between the GMPE analysis and four gridded SST analysis products: MUR, NCEI, OSTIA, CMC. The thick gray band is the globally-averaged uncertainty field from the GMPE product. The dashed line is a low-resolution version ( $\hat{T}_0^6$ ) of MUR (an intermediate product of the MRVA interpolation) which approximates the resolution of GMPE (with a  $0.25^\circ$  grid) better.

for the low-resolution sibling roughly approximates the ensemble spread, or the RMS difference averaged over *all* GMPE member products, which represents the analysis uncertainty in the GMPE SST product (light wide line). The RMS value for MUR ( $\hat{T}_0^9$ ) is higher than the value for its low-resolution sibling ( $\hat{T}_0^6$ ) by an average of approximately  $0.05^\circ\text{C}$ . This difference in RMS values is an indication of mean magnitude in the variability signal  $\hat{T}^6 + \hat{T}^7 + \hat{T}^8$ , which is missing in the low-resolution sibling. The high-resolution variability signal is plausibly perceived as “noise” by the lower-resolution reference analysis (GMPE) which by design does not resolve all the variability signal in MUR.

All curves in Fig. 7 show a prominent seasonal pattern. Specifically, the RMS differences and GMPE spread increase by  $0.1$  to  $0.2^\circ\text{C}$  during boreal summers, implying that the analysis uncertainty is generally high during the season for all the SST analysis products considered. To examine the seasonal behavior further, the RMS differences are computed excluding the Arctic Ocean (latitudes above  $65^\circ\text{N}$  in this paper) to avoid the highly variable patterns of summer-time warming in recent years (Steele and Dickinson, 2016). The resulting timeseries (Fig. 8) show much reduced summer-time peaks. Table 4 shows that the temporal maximum of the global RMS difference decreases by around  $0.1^\circ\text{C}$  for each analysis product if the Arctic Ocean is excluded. Outside of the Arctic, the time-averaged RMS difference for MUR and its low-resolution sibling  $\hat{T}_0^6$  are respectively  $0.36^\circ\text{C}$  and  $0.31^\circ\text{C}$ , while the corresponding value for GMPE spread (analysis uncertainty) is  $0.34^\circ\text{C}$ . The improved agreement among the SST analyses outside of the Arctic Ocean in boreal summer is an indication of general difficulty in performing SST analysis over the Arctic. An extensive comparison of nine analyses against independent buoy data from the Beaufort Sea (Castro et al., 2016) has confirmed large differences (sometimes in excess of  $2^\circ\text{C}$ ) among the analyzed SST values and shown that quantity (and possibly quality) of Arctic SST retrievals is a common issue among all global SST analyses including MUR. Persistent cloud cover in the boreal summer is noted as a leading cause of difficulty in SST analysis over the Arctic. The Arctic area is also found to be especially vulnerable to data

**Table 4**

Statistics of the time-series in Fig. 7 (“Entire Globe”) and in Fig. 8 (“Globe excluding Arctic”), which present the RMS difference to the GMPE SST analysis in Celsius (Kelvin). The analysis labeled “MUR-sibling” represents the low-resolution intermediate product  $\hat{T}_0^6$  (the dashed lines in the figures), while “GMPE-Spread” is the RMS difference averaged over all GMPE members (the wide grey lines in the figures) which is part of the GMPE product. All GMPE time-series examined here are over the period of 2010 through 2014. In addition, the bottom three rows of the table are analogous statistics of RMS differences between MUR and each of NCEI, OSTIA, and CMC products, for time-series over the indicated periods.

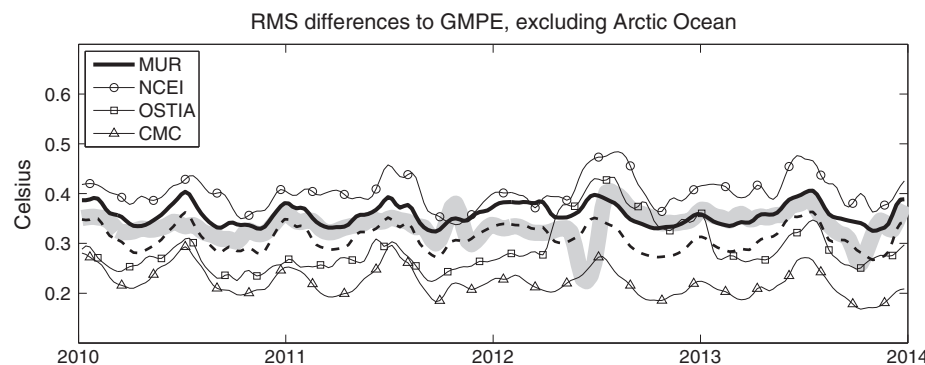
Analysis pair (for RMS difference)	Entire globe		Globe excluding Arctic	
	Maximum	Mean	Maximum	Mean
NCEI – GMPE	0.57	$0.42 \pm 0.05$	0.48	$0.40 \pm 0.03$
OSTIA – GMPE	0.53	$0.31 \pm 0.07$	0.43	$0.29 \pm 0.05$
CMC – GMPE	0.43	$0.25 \pm 0.06$	0.30	$0.22 \pm 0.03$
MUR – GMPE	0.54	$0.37 \pm 0.05$	0.41	$0.36 \pm 0.02$
MUR-sibling ( $\hat{T}_0^6$ ) – GMPE	0.51	$0.33 \pm 0.06$	0.36	$0.31 \pm 0.03$
GMPE-Spread (all members)	0.46	$0.34 \pm 0.04$	0.41	$0.34 \pm 0.03$
NCEI – MUR (2002–2014)	0.78	$0.55 \pm 0.09$	0.66	$0.52 \pm 0.06$
OSTIA – MUR (2007–2014)	0.70	$0.47 \pm 0.06$	0.57	$0.49 \pm 0.04$
CMC – MUR (2002–2014)	0.65	$0.42 \pm 0.09$	0.52	$0.39 \pm 0.04$

voids for the particular case of MODIS data and MUR that ingests them (Liu and Minnett, 2016) potentially due to the spatial and seasonal SST variability in the region induced in part by heat and freshness fluxes from river transports and ice melts.

#### 4.3. Feature resolutions

The stated resolution of a satellite retrieval data set typically correlates well with the resolution of the SST features found in the data. Fig. 9, left-panel, shows power spectral density (PSD) plots for several retrieval data sets, one data set from each data type ingested by MUR. Each PSD curve (computed along the satellite track) generally follows a random-walk power law (log-log slope of  $-2$ , thin straight dashed line)

**Fig. 8.** The same as Fig. 7, except that the spatial domain excludes the Arctic Ocean.





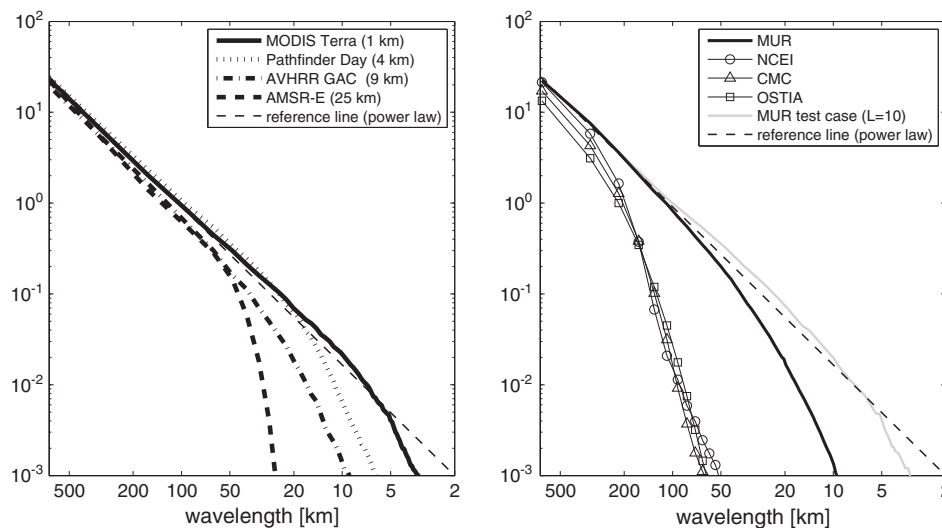


Fig. 9. Power spectral density plots of SST: satellite retrievals (left) and gridded analysis (right). The dashed straight lines are the random-walk power-law drawn in both plots as an identical reference.

until the drop-off at a wavelength around or slightly longer than the Nyquist interval which is twice the stated sampling interval: 1 km for MODIS, 4 km for Pathfinder, 9 km for AVHRR GAC, and 25 km for microwave.

In contrast, the grid resolution of an analysis product is a poor indicator of the nominal resolution of the features presented by the analyzed field. The analyzed SST feature resolution is often much lower than the grid resolution (Reynolds and Chelton, 2010; Reynolds et al., 2013) due to procedures that effectively impose smoothing such as widespread removal of “outlier” samples as well as high-wavenumber “noise”, interpolation over data voids of various sizes, and time-averaging over the “synoptic” period for the analysis. Indeed, the PSDs of the NCEI, CMC, and OSTIA analyses are remarkably similar to each other (right panel, Fig. 9) despite differences in their grid resolutions: 0.25° for NCEI, 0.20° for CMC, and 0.05° for OSTIA. Based on the PSDs, the feature resolution in these analysis products appears to be around 100 km.

On the other hand, MUR by design has much higher SST spectral contents (thick solid line, right panel) than the other analysis products. The MUR PSD drops off from the reference power law (dashed line) similarly to the 9-km AVHRR GAC retrieval sets. The PSD plots of the analysis products demonstrate that the grid resolution is only an indication of the maximum representable resolution which tend to be much higher than the actual feature resolution in all SST analysis products examined here, with MUR displaying a feature resolution an order of magnitude higher than the others.

The MRVA interpolation parameters can be adjusted to increase apparent feature resolution in the analysis. The gray line in Fig. 9, labeled “MUR test case”, is the PSD of an analysis produced with the same input data as MUR. The test case is produced with the same MRVA parameters as MUR except that all the regularization weights are reduced to quarter of the original values and the scale parameter is raised from  $L = 9$  to  $L = 10$ . The figure shows similarity between the PSDs of the test case and MODIS data. Despite the similarity in PSD, the test case is found to have substantially larger data residuals. In particular, the RMS residuals of the MODIS Terra and Aqua for the test case have increased by twofolds, from 0.36°C to 0.72°C in both data sets, during a study period 2015–2016. Scale-dependent comparison of input data residuals between siblings of the test case and those of MUR also reveals that the disparity in the RMS residuals increases as the resolution  $L$  increases. These indicate that the “test case” analysis is substantially inferior to MUR in representation of the input SST features, especially the high resolution features in MODIS. Numerical conditioning of the inversion steps in MRVA due to an inadequate level of regularization is a potential cause of the substantially large interpolation residuals in the

test case. These results justify the use of a lower feature resolution parameter ( $L = 9$ ) for MUR than what the  $0.01^\circ \times 0.01^\circ$  grid can accommodate ( $L = 10$ ).

We note that the grid resolution higher than the feature resolution is still useful in presenting the location of SST features. The PSD analysis is only a spatially averaged summary based on Fourier decomposition insensitive to feature locations. Given a structure with a certain wavenumber, the sub-wavelength grid points are necessary to present the local phase of the structure precisely. The global distribution of high-wavenumber SST features is also geographically dependent, with prominent sub-mesoscale structures tending to concentrate around the dynamic zones associated with strong currents, wind, and upwelling (e.g., SST fronts; Fig. 3 in Obenour, 2013).

#### 4.4. Comparison to VIIRS retrieval data

To examine the high-resolution SST features in MUR, MUR and its siblings are compared to coincident VIIRS retrieval data. The 3000 km-wide swath of VIIRS is advantageous for capturing spatial patterns, and VIIRS data are not ingested by the current version of MUR. The VIIRS data set used here is produced by the Naval Oceanographic Office (NAVO) as a GHRSSST collection and is quality-controlled and pre-processed the same way as the MODIS data sets ingested by MUR. The NAVO VIIRS data are available since mid-2013. Another option for validation of the high-resolution SST features is comparison to the regional SST retrievals from the latest geostationary satellites including GOES-R and Himawari-8 offering 2-km resolution SST fields from infrared sensors (Kurihara et al., 2016). Such comparison is underway and is not covered in this paper.

Fig. 10 shows scale-dependent data residuals for the VIIRS and MODIS data sets from a coincident period (2015–2016). A monotonic decrease in the RMS data residual as a function of the analysis scale  $L$  would support consistency in SST features between MUR and the data set at all scales. The MODIS data residuals indeed decrease monotonically (solid lines). The decrease in the VIIRS residual, however, diminishes once the resolution reaches  $L = 7$  where a relatively shallow minimum is observed (dotted line). Existence of the residual minimum for the VIIRS data supports the choice of an analysis scale  $L$  smaller than the maximum offered by the MUR grid ( $L = 10$ ), although the choice for the current version of MUR ( $L = 9$ ) is not at the minimum VIIRS residual.

Since the ingested MODIS data are solely responsible for the high-resolution features in MUR, consistency in the SST features between the MODIS and VIIRS data would directly affect our evaluation based on VIIRS data. Fig. 10 indicates that, in terms of the RMS residuals, MUR

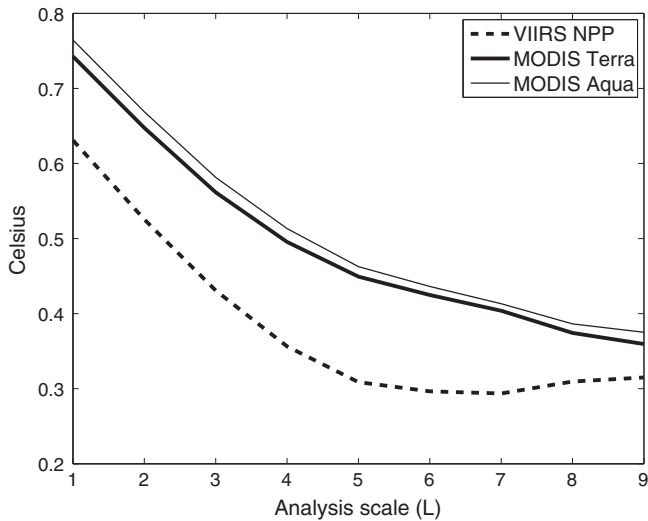


Fig. 10. The same as Fig. 6, except that a VIIRS retrieval data set is included in the comparison and that the comparison period is from year 2015 to 2016 instead of 2002 to 2013.

agrees with VIIRS better than MODIS at all scales. It is not surprising that VIIRS shows a smaller data residual than MODIS even though MUR does not ingest VIIRS, because MUR ingests other non-MODIS data. In particular, the residuals for the AVHRR GAC data ingested by MUR are

also smaller than the MODIS residuals (Table 3) and are relatively close to the VIIRS residual. For some meso-scales ( $L = 4, 5, 6$ ), the VIIRS residuals are more than  $0.1^{\circ}\text{C}$  smaller than MODIS residuals. The difference in the residuals indicates that VIIRS has different meso-scale features from MODIS, and this in turn makes direct comparison of the finer scale features difficult between VIIRS and MODIS data sets due to the much smaller magnitudes of the finer scale features (Fig. 9). Fig. 11 displays examples of coincident mesoscale SST patterns from the VIIRS and MODIS data sets, based on the samples flagged as the highest quality. Some common patterns of data voids can be seen due to atmospheric conditions like cloud cover. Significant differences in sampling patterns (for the highest quality samples) can also be found. Differences in mesoscale SST patterns can indeed be noted in areas such as the lower-left corners of the VIIRS and MODIS-Aqua fields where more specular patterns are found in the VIIRS data.

Validation of the high-resolution features in MUR by direct comparison to the VIIRS data appears to be difficult due to the differences in larger-scale (particularly meso-scale) features between VIIRS and MODIS data sets. Two other VIIRS retrieval data sets (also as GHRSSST collections) have become available after the NAVO version. One is based on the Advanced Clear Sky Processor for Oceans (ACSPO) retrieval algorithm from NOAA's Office of Satellite and Product Operations (OSPO), and the other is based on the RSMAS algorithm implemented at OBPG. The VIIRS data residuals computed using the OSPO and OBPG versions are found to display similar scale-dependencies as the NAVO version, including closer agreement with MUR in the mesoscale range than the MODIS data ingested by MUR.

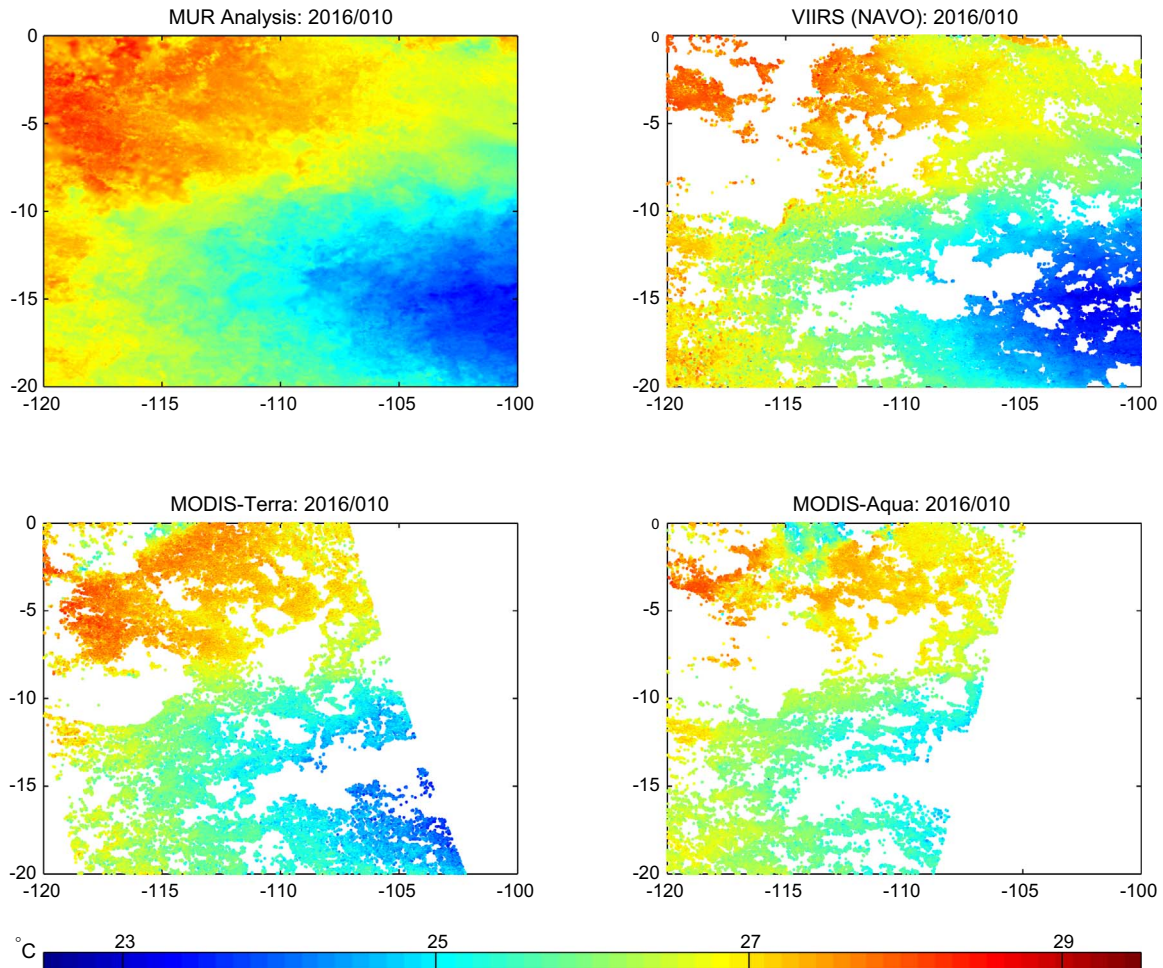


Fig. 11. SST pattern in a  $20^{\circ} \times 20^{\circ}$  area from the MUR analysis (top-left), NAVO VIIRS retrievals (top-right), JPL MODIS-Terra retrievals (bottom-left), and JPL MODIS-Aqua retrievals (bottom-right). Only the highest-quality retrieval samples are shown. The MUR analysis has ingested the MODIS retrievals but not VIIRS.

## 5. Summary and future prospects

The MUR global SST analysis ingests the 1-km resolution MODIS SST retrieval data sets and presents an estimate of the foundation SST estimates on a  $0.01^\circ \times 0.01^\circ$  grid. MUR improves the analyzed feature resolution by an order of magnitude over most of the existing SST analysis products, from approximately 100 km down to 10 km. At mesoscale resolutions, MUR agrees with the  $0.25^\circ \times 0.25^\circ$ -gridded GMPE median SST analysis to  $0.36^\circ\text{C}$  on average, except in summer-time Arctic region (latitudes higher than  $65^\circ\text{N}$ ) where differences among the existing SST analyses are known to be relatively large (e.g., Castro et al., 2016).

MUR simultaneously manages reconstruction of 1 km-scale SST features and interpolation over larger-scale data voids using the MRVA interpolation method (Fig. 2). The MRVA method is based on an energy-preserving and reversible multi-scale transform that allows simultaneous use of multiple interpolation length scales. The multi-scale decomposition allows MUR to use multiple synoptic time periods including the 5-day data window for reconstruction of mesoscale features and data windows of only few hours for the smaller scale features. The use of scale-dependent data windows is essential for accurate representation of sub-mesoscale features (Fig. 5) which tend to evolve faster than larger features. Optimization of the MRVA interpolation parameters such as the data window lengths is a topic of investigation in planning.

The MRVA method is also a “mesh-less” interpolation procedure that avoids truncation of the geolocation information in the input data and preserves intra-grid features like SST front location relatively well (Chin et al., 2014). Validation of high-resolution features in the MUR SST analysis is still an ongoing work. The inter-product comparison results presented in this paper are associated with only the latest MUR version 4.1. Comparisons of MUR to independent VIIRS data so far have been inconclusive in validating the analyzed high-resolution SST patterns because differences in meso-scale patterns between VIIRS and MODIS are large enough in magnitude to overwhelm feature comparison at smaller-scales. A careful scale-based decomposition of the reference data (in this case VIIRS) might be necessary for proper examination of the high-resolution patterns in MUR. Comparison to independent oceanic front data sets is also under consideration.

A future version of MUR plans to ingest VIIRS data to complement the MODIS data in spatial coverage of high-resolution SST retrievals. It also looks to update the input data, especially with respect to the skin-to-bulk bias estimation since the lack of SSES bias in the early MODIS and Pathfinder data sets is linked to the relatively large analysis residuals for these data. Other considerations for a future version include: use of day-time MODIS (and VIIRS) retrievals along with their nighttime counterparts to further improve high-resolution coverage, and use of an external reference SST field (instead of one constructed solely from the input data) to improve outlier detection. Improvement in the Arctic analysis is a common issue shared by other existing SST analysis products.

## Acknowledgments

The research described in this paper was carried out at the Jet Propulsion Laboratory (JPL), California Institute of Technology, under a contract with the National Aeronautics and Space Administration (NASA), mostly through the Making Earth System Data Records for Use in Research Environments (MEaSUREs) program. The Physical Oceanography Distributed Active Archive Center (PO.DAAC) at JPL provided logistical supports for the production of the MUR SST product. Dr. Dimitris Menemenlis of JPL provided the ECCO2 simulated SST fields used for validation.

## References

- Alparone, L.L., Aiazzi, B.B., Baronti, S.S., Garzelli, A.A., 2015. Remote Sensing Image Fusion. CRC Press, Boca Raton, Florida.
- Andersen, S.S., Tonboe, R.R., Kern, S.S., Schyberg, H.H., 2006. Improved retrieval of sea ice total concentration from spaceborne passive microwave observations using numerical weather prediction model fields: an intercomparison of nine algorithms. *Remote Sens. Environ.* 104, 374–392.
- Bashmachnikov, I.I., Boutov, D.D., Dias, J.J., 2013. Manifestation of two meddies in altimetry and sea-surface temperature. *Ocean Sci.* 9, 249–259.
- Battle, G.G., 1987. A block spin construction of ondelettes. Part I: Lemarié functions. *Commun. Math. Phys.* 110, 601–615.
- Baylis, A.A., Orben, R.R., Pistorius, P.P., Brickle, P.P., Staniland, I.I., Ratcliffe, N.N., 2015. Winter foraging site fidelity of king penguins breeding at the Falkland Islands. *Mar. Biol.* 162, 99–110.
- Bookstein, F.L.F.L., 1989. Principal warps: thin-plate splines and the decomposition of deformations. *IEEE Trans. Pattern Anal. Mach. Intell.* 11, 567–585.
- Brasnett, B.B., 2008. The impact of satellite retrievals in a global sea-surface-temperature analysis. *Q. J. R. Meteorol. Soc.* 134, 1745–1760.
- Breivik, L.A.L.A., Eastwood, S.S., Godoy, O.O., Schyberg, H.H., Andersen, S.S., Tonboe, R.R.T., 2001. Sea ice products for EUMETSAT satellite application facility. *Can. J. Remote. Sens.* 27 (5), 403–410.
- Casey, K.S.K.S., Brandon, T.B.T.B., Cornillon, P.P., Evans, R.R., 2010. The past, present and future of the AVHRR Pathfinder SST Program. In: Barale, V.V., Gower, J.J., Alberotanza, L.L. (Eds.), *Oceanography from Space: Revisited*. Springer.
- Castro, S.L.S.L., Wick, G.A.G.A., Steele, M.M., 2016. Validation of satellite sea surface temperature analyses in the Beaufort Sea using UpTempO buoys. *Remote Sens. Environ.* 187, 458–475.
- Chen, K.K., Gawarkiewicz, G.G., Kwon, Y.O.Y.O., Zhang, W.G.W.G., 2015. The role of atmospheric forcing versus ocean advection during the extreme warming of the Northeast U.S. continental shelf in 2012. *J. Geophys. Res.* 120, 4324–4339.
- Chin, T.M.T.M., Milliff, R.F.R.F., Large, W.G.W.G., 1998. Basin-scale, high-wavenumber sea-surface wind fields from a multiresolution analysis of scatterometer data. *J. Atmos. Oceanic Tech.* 15, 741–763.
- Chin, T.M.T.M., Vazquez-Cuervo, J.J., Armstrong, E.M.E.M., 2014. On “gridless” interpolation and subgrid data density. *J. Atmos. Oceanic Tech.* 31, 1642–1652.
- Chui, C.K.C.K., Wang, J.Z.J.Z., 1991. A cardinal spline approach to wavelets. *Proc. Am. Math. Soc.* 113, 785–793.
- Dash, P.P., Ignatov, A.A., Kihai, Y.Y., Sapper, J.J., 2010. The SST quality monitor (SQUAM). *J. Atmos. Oceanic Tech.* 27 (11), 1899–1917.
- Dash, P.P., Ignatov, A.A., Martin, M.M., Donlon, C.C., Brasnett, B.B., Reynolds, R.W.R.W., Banzon, V.V., Beggs, H.H., Cayula, J.F.J.F., Chao, Y.Y., Grumbine, R.R., Maturi, E.E., Harris, A.A., Mittaz, J.J., Sapper, J.J., Chin, T.M.T.M., Vazquez, J.J., Armstrong, E.M.E.M., Gentemann, C.C., Cummings, J.J., Fiolle, J.F.J.F., Autret, E.E., Roberts-Jones, J.J., Ishizaki, S.S., Hoyer, J.L.J.L., Poulter, D.D., 2012. Group for high resolution sea surface temperature (GHRST) analysis fields inter-comparisons Part 2: near real time web-based level 4 SST quality monitor (L4-SQUAM). *Deep-Sea Res. II Top. Stud. Oceanogr.* 77, 31–43.
- Daubechies, I.I., 1992. Ten Lectures on Wavelets. Society for Industrial and Applied Mathematics, Philadelphia.
- Donlon, C.C., Robinson, I.I., Casey, K.S.K.S., Vazquez-Cuervo, J.J., Armstrong, E.E., Arino, O.O., Gentemann, C.C., et al., 2007. The global ocean data assimilation experiment high-resolution sea surface temperature pilot project. *Bull. Amer. Meteor. Soc.* 88, 1197–1213.
- Donlon, C.J.C.J., Martin, M.M., Stark, J.D.J.D., Roberts-Jones, J.J., Fiedler, E.E., Wimmer, W.W., 2012. The operational sea surface temperature and sea ice analysis (OSTIA) system. *Remote Sens. Environ.* 116, 140–158.
- Donlon, C.J.C.J., Minnett, P.J.P.J., Gentemann, C.C., Nightingale, T.J.T.J., Barton, I.J.I.J., Ward, B.B., M.M., J.J., 2002. Toward improved validation of satellite sea surface skin temperature measurements for climate research. *J. Climate* 15, 353–369.
- Frey, R.A.R.A., Ackerman, S.A.S.A., Liu, Y.Y., Strabala, K.I.K.I., Zhang, H.H., Key, J.R.J.R., Wang, X.X., 2008. Cloud detection with MODIS. Part I: improvements in the MODIS cloud mask for collection 5. *J. Atmos. Oceanic Tech.* 25, 1057–1072.
- Gentemann, C.L.C.L., Fewings, M.R.M.R., Garcia-Reyes, M.M., 2017. Satellite sea surface temperatures along the west coast of the United States during the 2014–2016 northeast Pacific marine heat wave. *Geophys. Res. Lett.* 44, 312–319.
- Goela, P.C.P.C., Danchenko, S.S., Icely, J.D.J.D., Lubian, L.M.L.M., Cristina, S.S., Newton, A.A., 2014. Using CHEMTAX to evaluate seasonal and interannual dynamics of the phytoplankton community off the south-west coast of Portugal. *Estuar. Coast. Shelf Sci.* 151, 112–123.
- Hurrell, J.W.J.W., Hack, J.J.J.J., Shea, D.D., Caron, J.M.J.M., Rosinski, J.J., 2008. A new sea surface temperature and sea ice boundary dataset for the Community Atmosphere Model. *J. Climate* 21, 5145–5153.
- Ignatov, A.A., Zhou, X.X., Petrenko, B.B., Liang, X.X., Kihai, Y.Y., Dash, P.P., Stroup, J.J., Sapper, J.J., DiGiacomo, P.P., 2016. AVHRR GAC SST reanalysis version 1 (RAN1). *Remote Sens.* 8 (4), 315.
- Inoue, H.H., 1986. A least-squares smooth fitting for irregularly spaced data: finite-element approach using the cubic B-spline basis. *Geophysics* 51, 2051–2066.
- Iwasaki, S.S., Isobe, A.A., Kako, S.S., 2014. Atmosphere-ocean coupled process along coastal areas of the Yellow and East China Seas in winter. *J. Climate* 27, 155–167.
- Kaplan, A.A., Cane, M.M., Kushnir, Y.Y., 2003. Reduced space approach to the optimal analysis of historical marine observations: accomplishments, difficulties, and prospects. In: *Advances in the Applications of Marine Climatology*. World Meteorological Organization. WMO/TD-No. 1081 (JCOMM Technical Report No. 13), pp. 199–216.
- Kawai, Y.Y., Wada, A.A., 2007. Diurnal sea surface temperature variation and its impact



- on the atmosphere and ocean: a review. *J. Oceanogr.* 63, 721–744.
- Kilpatrick, K.A.K.A., Podesta, G.P.G.P., Evans, R.R., 2001. Overview of the NOAA/NASA advanced very high resolution radiometer Pathfinder algorithm for sea surface temperature and associated matchup database. *J. Geophys. Res.* 106 (C5), 9179–9197.
- Kurihara, Y.Y., Murakami, H.H., Kachi, M.M., 2016. Sea surface temperature from the new Japanese geostationary meteorological Himawari-8 satellite. *Geophys. Res. Lett.* 43, 1234–1240.
- Lemarié, P.G.P.G., 1988. Ondelettes à localisation exponentielles. *J. Math. Pures et Appl.* 67, 227–236.
- Liu, L.L., Lozano, C.C., Iredell, D.D., 2015. Time-space SST variability in the Atlantic during 2013: Seasonal cycle. *J. Atmos. Oceanic Tech.* 32, 1689–1705.
- Liu, Y.Y., Minnett, P.J.P.J., 2016. Sampling errors in satellite-derived infrared sea-surface temperatures Part I: global and regional MODIS fields. *Remote Sens. Environ.* 177, 48–64.
- Mallat, S.G.S.G., 1989. A theory for multiresolution signal decomposition: the wavelet representation. *IEEE Trans. Pattern Anal. Mach. Intell.* 11, 674–693.
- Martin, M.M., Dash, P.P., Ignatov, A.A., Banzon, V.V., Beggs, H.H., Brasnett, B.B., Cayula, J.J., Cummings, J.J., Donlon, C.C., Gentemann, C.C., Grumbine, R.R., Ishizaki, S.S., Maturi, E.E., Reynolds, R.W.R.W., Roberts-Jones, J.J., 2012. Group for high resolution sea surface temperature (GHRST) analysis fields inter-comparisons. Part 1: a GHRST multi-product ensemble (GMPE). *Deep-Sea Res.* II 77–80, 21–30.
- Menemenlis, D.D., Campin, J.M.J.M., Heimbach, P.P., Hill, C.C., Lee, T.T., Nguyen, A.A., Schodlok, M.M., Zhang, H.H., 2008. ECCO2: high resolution global ocean and sea ice data synthesis. *Mercator Ocean Q. Newsl.* 31, 13–21.
- Merchant, C.C., Harris, A.A., Roquet, H.H., Le Borgne, P.P., 2009. Retrieval characteristics of non-linear sea surface temperature from the advanced very high resolution radiometer. *Geophys. Res. Lett.* 36. <http://dx.doi.org/10.1029/2009GL039843>.
- Mill, G.N.G.N., da Costa, V.S.V.S., Lima, N.D.N.D., Gabioux, M.M., Guerra, L.A.A.L.A.A., Paiva, A.M.A.M., 2015. Northward migration of Cape Sao Tome rings, Brazil. *Cont. Shelf Res.* 106, 27–37.
- Morak-Bozzo, S.S., Merchant, C.C., Kent, E.E., Berry, D.D., Carella, G.G., 2016. Climatological diurnal variability in sea surface temperature characterized from drifting buoy data. *Geosci. Data J.* 3, 20–28.
- Nidzieko, N.J.N.J., Largier, J.L.J.L., 2013. Inner shelf intrusions of offshore water in an upwelling system affect coastal connectivity. *Geophys. Res. Lett.* 40, 5423–5428.
- Obenour, K.M.K.M., 2013. Temporal Trends in Global Sea Surface Temperature Fronts. University of Rhode Island, Department of Oceanography. <http://digitalcommons.uri.edu/theses/136/> Master's thesis.
- O'Carroll, A.G.A.G., Blackmore, T.T., Fennig, K.K., Saunders, R.W.R.W., Millington, S.S., 2012. Towards a bias correction of the AVHRR Pathfinder SST data from 1985 to 1998 using ATSR. *Remote Sens. Environ.* 116, 118–125.
- Petrenko, B.B., Ignatov, A.A., Kihai, Y.Y., Stroup, J.J., Dash, P.P., 2014. Evaluation and selection of SST regression algorithms for JPSS VIIRS. *J. Geophys. Res. Atmos.* 119, 4580–4599.
- Press, W.H.W.H., Rybicki, G.B.G.B., 1989. Fast algorithm for spectral analysis of unevenly sampled data. *Astrophys. J.* 338, 277–280.
- Ray, R.D.R.D., Susanto, R.S.R.S., 2016. Tidal mixing signatures in the Indonesian seas from high-resolution sea surface temperature data. *Geophys. Res. Lett.* 43. <http://dx.doi.org/10.1002/2016GL069485>.
- Rayner, N.A.N.A., Parker, D.E.D.E., Horton, E.B.E.B., Folland, C.K.C.K., Alexander, L.V.L.V., Rowell, D.P.D.P., Kent, E.C.E.C., Kaplan, A.A., 2003. Global analyses of sea surface temperature, sea ice, and night marine air temperature since the late nineteenth century. *J. Geophys. Res.* 108 (D14), 4407. <http://dx.doi.org/10.1029/2002JD002670>.
- Reynolds, R.W.R.W., Chelton, D.B.D.B., 2010. Comparisons of daily sea surface temperature analyses for 2007–08. *J. Climate* 23, 3545–3562.
- Reynolds, R.W.R.W., Chelton, D.B.D.B., Roberts-Jones, J.J., Martin, M.J.M.J., 2013. Objective determination of feature resolution in two sea surface temperature analyses. *J. Climate* 26, 2514–2533.
- Reynolds, R.W.R.W., Rayner, N.A.N.A., Smith, T.M.T.M., Stokes, D.C.D.C., Wang, W.W., 2002. An improved in situ and satellite SST analysis for climate. *J. Climate* 15, 1609–1625.
- Reynolds, R.W.R.W., Smith, T.M.T.M., 1994. Improved global sea surface temperature analyses using optimum interpolation. *J. Climate* 7, 929–948.
- Reynolds, R.W.R.W., Smith, T.M.T.M., Liu, C.C., Chelton, D.B.D.B., Casey, K.S.K.S., Schlax, M.G.M.G., 2007. Daily high-resolution-blended analyses for sea surface temperature. *J. Climate* 20, 5473–5496.
- Scales, K.L.K.L., Miller, P.I.P.I., Varo-Cruz, N.N., Hodgson, D.J.D.J., Hawkes, L.A.L.A., Godley, B.J.B.J., 2015. Oceanic loggerhead turtles *Caretta caretta* associate with thermal fronts: evidence from the Canary Current Large Marine Ecosystem. *Mar. Ecol. Prog. Ser.* 519, 195–207.
- Steele, M.M., Dickinson, S.S., 2016. The phenology of arctic ocean surface warming. *J. Geophys. Res. Oceans* 121, 6847–6861.
- Steele, M.M., Zhang, J.J., Ermold, W.W., 2010. Mechanisms of summertime upper arctic ocean warming and the effect on sea ice melt. *J. Geophys. Res. Oceans* 115. <http://dx.doi.org/10.1029/2009JC005849>.
- Turrent, C.C., Zaitsev, O.O., 2014. Seasonal cycle of the near-surface diurnal wind field over the Bay of La Paz, Mexico. *Bound.-Lay. Meteorol.* 151, 353–371.
- Unser, M.M., 1997. Ten good reasons for using spline wavelets. *Proc. SPIE* 3169, 422–431.
- Vazquez, J.J., Dewitte, B.B., Chin, T.M.T.M., Armstrong, E.M.E.M., Purca, S.S., Alburquerque, E.E., 2013. An analysis of SST gradients off the Peruvian coast: the impact of going to higher resolution. *Remote Sens. Environ.* 131, 76–84.
- Wiafe, G.G., Nyadjro, E.E., 2015. Satellite observations of upwelling in the Gulf of Guinea. *IEEE Geosci. Remote Sens. Lett.* 12 (5), 1066–1070.
- Wornell, G.W.G.W., 1993. Wavelet-based representations for the 1/f family of fractal processes. *Proc. IEEE* 81, 1428–1450.
- Xu, F.F., Ignatov, A.A., 2010. Evaluation of in situ sea surface temperatures for use in the calibration and validation of satellite retrievals. *J. Geophys. Res.* 115, C09022. <http://dx.doi.org/10.1029/2010JC006129>.